

# Tetrazine-enhanced donor-acceptor-donor metal-organic frameworks for photodynamic antibacterial therapy and wound healing

Received: 25 November 2024

Accepted: 16 October 2025

Published online: 25 November 2025

 Check for updates

Yanzhao Chen<sup>1,4</sup>, Yangyin Xue<sup>1,4</sup>, Xiaowei Xu<sup>1</sup>, Yu Su<sup>1</sup>, Xidan Tong<sup>1</sup>, Long Zhu<sup>1</sup>, Yifei Zuo<sup>1</sup>, Chao Ban<sup>1</sup>, Jiakuan Chen<sup>1</sup>, Wancai Que<sup>1,2</sup>  , Yueqin Zheng<sup>1,3</sup>   & Weiwei Guo<sup>1,2</sup>  


Multidrug-resistant infections and impaired healing in chronic diabetic wounds are major clinical challenges. Photodynamic therapy (PDT) is a promising alternative, but its efficacy is limited by conventional photosensitizers. Here, we design two donor-acceptor-donor (D-A-D) metal-organic frameworks (MOFs) using a tetrazine core to narrow the band gap, which enhances visible-light-driven reactive oxygen species (ROS) generation. These MOFs exhibit superior photocatalytic antibacterial activity over benchmark materials. After functionalization with L-arginine, the resulting composites (e.g., A@Zn-TDP) co-release ROS, nitric oxide (NO), and reactive nitrogen species (RNS) enabling rapid and broad-spectrum bacterial eradication (including against MRSA) at low concentrations (25 µg/mL) while accelerating tissue regeneration. In a male diabetic mouse model, A@Zn-TDP treatment under light reduces bacterial load by >95%, controls inflammation, promotes angiogenesis, and speeds up wound closure. This study establishes tetrazine-based D-A-D MOFs as a rationally designed platform for effective PDT and wound healing, underscoring their clinical translational potential.

Bacterial infections pose an escalating global health crisis, further compounded by the relentless rise of antimicrobial resistance (AMR)<sup>1–3</sup>. In 2019 alone, bacterial infections were responsible for an estimated 13.7 million deaths worldwide, with *Staphylococcus aureus* (*S. aureus*) and *Escherichia coli* (*E. coli*) identified as leading culprits and major contributors to AMR-associated mortality<sup>4–6</sup>. Particularly alarming is methicillin-resistant *S. aureus* (MRSA)<sup>7,8</sup>, which accounted for over 100,000 deaths that year, its prevalence driven by antibiotic overuse and a stagnating antibiotic development pipeline<sup>2,9</sup>. Beyond systemic infections, bacterial colonization at local sites promotes robust biofilm formation<sup>10</sup>. These dense extracellular polymeric

substance (EPS) matrices act as formidable barriers, shielding pathogens from host immune responses and impeding the penetration of antimicrobial agents<sup>11–13</sup>. This problem is especially acute in chronic wounds such as diabetic ulcers, where the exposed wound bed fosters recurrent infections and the pathological microenvironment perpetuates persistent inflammation, severely delaying healing and recovery<sup>14–16</sup>.

Confronting these challenges demands innovative strategies that extend beyond conventional antibiotics. Photodynamic therapy (PDT) has emerged as a promising non-antibiotic approach, leveraging light-activated photosensitizers (PSs) to generate reactive oxygen species

<sup>1</sup>School of Science, China Pharmaceutical University, Nanjing, China. <sup>2</sup>Phase I Clinical Trial Unit, Fujian Medical University Union Hospital, Fuzhou, China.

<sup>3</sup>Center of Drug Discovery, State Key Laboratory of Natural Medicine, China Pharmaceutical University, Nanjing, China. <sup>4</sup>These authors contributed equally: Yanzhao Chen, Yangyin Xue.  e-mail: [wancaiQue@fjmu.edu.cn](mailto:wancaiQue@fjmu.edu.cn); [yzheng@cpu.edu.cn](mailto:yzheng@cpu.edu.cn); [guoweimei@cpu.edu.cn](mailto:guoweimei@cpu.edu.cn)

(ROS) capable of inducing peroxidative damage and bacterial membrane disruption<sup>17–19</sup>. However, clinically approved PSs—primarily porphyrin derivatives such as phthalocyanines<sup>20,21</sup>, porphyrin<sup>22</sup> and BODIPY<sup>23</sup> derivatives—are constrained by poor aqueous solubility, aggregation-induced quenching, and suboptimal ROS generation efficiency, ultimately limiting their therapeutic utility<sup>24–26</sup>. In recent years, metal-organic frameworks (MOFs) have gained attention as potent PDT platforms due to their tunable metal nodes and organic linkers, which enable intrinsic PS incorporation<sup>27,28</sup>. Their robust crystalline architectures facilitate efficient light capture and rapid energy transfer, while their inherent porosity allows them to serve as nano-carriers for co-loaded therapeutics<sup>29</sup>. However, widely studied photosensitive MOFs, such as PCN-224<sup>30</sup> and NH<sub>2</sub>-MIL-125(Ti)<sup>31</sup>, continue to exhibit insufficient ROS generation, restricting their antibacterial efficacy against resilient infections. Overcoming these limitations necessitates rational engineering of MOF architectures to enhance photosensitizing efficiency and stability.

A central strategy in this engineering endeavor involves optimizing the pathways for ROS generation. Upon light activation, PSs within MOFs transition from ground to excited singlet states, followed by intersystem crossing (ISC) to long-lived triplet states—an essential process for efficient ROS generation<sup>32</sup>. Designing donor-acceptor (D-A-D) architectures effectively reduces the ISC energy gap, promoting charge separation and prolonging triplet-state lifetimes to enhance photocatalytic ROS production<sup>33</sup>. Furthermore, increasing the electron-donating character of donors or the electron-deficiency of acceptors can substantially boost ISC efficiency while minimizing non-radiative losses, thereby elevating ROS quantum yields. Recent advances in D-A-D covalent organic frameworks (COFs) have validated these design principles through acceptor fine-tuning<sup>34,35</sup>. However, despite their promise, D-A-D MOFs remain scarce due to challenges in ligand conjugation control and the limited availability of suitable acceptor groups required for constructing efficient photocatalytic MOFs<sup>36</sup>.

Here, we propose a design strategy by integrating tetrazine—a readily available, biocompatible, and strong electron acceptor—into D-A-D MOFs to help overcome existing PDT limitations. We report the development of two D-A-D photosensitive MOFs, Zn-TDP and Ni-TDP, synthesized using a pyrazole-tetrazine-pyrazole (TDP) ligand. This represents the demonstration of tetrazine as a powerful electron-accepting moiety within D-A-D MOF architectures, engineered to boost ISC efficiency and improve photocatalytic ROS generation. Coordination of Zn<sup>2+</sup> or Ni<sup>2+</sup> to pyrazole nitrogen atoms yields stable three-dimensional porous frameworks (Fig. 1). Harnessing their structural stability and porosity, we further fabricate therapeutic composites by incorporating L-arginine (L-Arg) forming A@Zn-TDP and A@Ni-TDP. These systems exploit photodynamically generated ROS to trigger nitric oxide (NO) release from L-Arg. The released NO penetrates biofilms and reacts with ROS to form reactive nitrogen species (RNS) such as peroxyxynitrite (ONOO<sup>-</sup>)<sup>37</sup>, exerting potent bactericidal effects while orchestrating a biphasic immune response—enhancing pro-inflammatory clearance during infection and facilitating the transition to anti-inflammatory phases. The A@Zn-TDP effectively eradicates MRSA infections both *in vitro* and *in vivo* at low concentrations (25 µg/mL), demonstrating enhanced therapeutic efficacy compared to most existing ROS/NO-based systems. Critically, this represents the application of D-A-D MOFs in biomedicine with photodynamic antibacterial efficacy surpassing classical photosensitive MOFs. This tetrazine-driven D-A-D design expands the frontier for developing advanced photosensitizers and establishes a versatile platform for on-demand photodynamic antibacterial therapy, thereby offering a promising solution to eradicate refractory infections and accelerate chronic wound healing in diabetic complications.

## Results and discussion

### Synthesis and characterizations

Zn-TDP and Ni-TDP were synthesized via solvothermal reactions of H<sub>2</sub>TDP with either zinc acetate or nickel acetate in N,N-dimethylformamide (DMF) or DMF/H<sub>2</sub>O mixtures (Fig. 2a). Powder X-ray diffraction (PXRD) analysis confirmed the crystallinity of both frameworks, revealing well-defined diffraction patterns consistent with their simulated structures (Fig. 2b, c). In Zn-TDP, each zinc atom is tetrahedrally coordinated to four nitrogen atoms from H<sub>2</sub>TDP ligands, forming stable one-dimensional chains interconnected through pyrazole groups—a structural motif analogous to Zn-BDP (where zinc ions are bridged by pyrazole-benzene-pyrazole linkers)<sup>38</sup>. Likewise, the PXRD pattern of Ni-TDP matched both its simulated structure and that of Ni-BDP, indicating the successful formation of a robust framework<sup>39</sup>. Specifically, each Ni<sup>2+</sup> ion coordinates to three nitrogen atoms from TDP pyrazole groups and three oxygen atoms from μ<sub>4</sub>-OH/μ<sub>4</sub>-OH<sub>2</sub> moieties, yielding a stable framework with fcu topology. The distinct MOF architectures may arise from differences in the coordination preferences of the metal nodes (Zn<sup>2+</sup> *vs.* Ni<sup>2+</sup>), variations in crystal growth kinetics and thermodynamic stability, as well as differences in synthetic conditions.

Inductively coupled plasma mass spectrometry (ICP-MS) quantified the metal content at 11.25 ± 0.08% for zinc in Zn-TDP and 16.19 ± 0.04% for nickel in Ni-TDP (Supplementary Table 1), reflecting differences in metal coordination environments during MOF self-assembly. Both Zn-TDP and Ni-TDP demonstrated exceptional structural stability, maintaining their crystallinity even after five days of immersion in PBS (Supplementary Fig. 1). This durability arises from the strong coordination interactions between Zn<sup>2+</sup>/Ni<sup>2+</sup> (soft acids) and pyrazolate ligands (soft bases), consistent with the hard-soft acid-base principle. Further structural characterization via N<sub>2</sub> adsorption isotherms at 77 K revealed type I behavior for both MOFs, indicative of their microporous nature (Supplementary Fig. 2). Zn-TDP and Ni-TDP exhibited Brunauer–Emmett–Teller (BET) surface areas of 252.74 m<sup>2</sup>g<sup>-1</sup> and 858.86 m<sup>2</sup>g<sup>-1</sup>, respectively, with corresponding pore sizes of 0.84 nm and 0.82 nm. This microporous architecture not only confers high porosity but also renders them effective carriers for drug loading, underscoring their potential as versatile platforms for advanced biomedical applications.

The FT-IR spectra of Zn-TDP and Ni-TDP are shown in Fig. 2d. The strong peaks observed in the 1400–1600 cm<sup>-1</sup> range indicated the presence of C=C, C=N and N=N stretching vibrations from the tetrazine and pyrazolate rings<sup>40</sup>. The weak peak at 507/508 cm<sup>-1</sup> in the Zn-TDP/Ni-TDP spectrum corresponded to Zn-N/Ni-N stretching vibrations<sup>41</sup>. Transmission electron microscopy (TEM, Fig. 2e, 2f) reveals distinct morphologies: Zn-TDP forms rod-like nanostructures with widths below 50 nm, whereas Ni-TDP appears as quasi-spherical nanoparticles approximately 20 nm in size. This morphological difference is attributed to variations in the coordination ratios between the Zn/Ni atoms and the pyrazole N atoms, leading to distinct coordination topologies. Elemental mapping by energy dispersive spectroscopy (EDS) confirmed the uniform distribution of Zn, Ni, C, and N within their respective frameworks. Further analysis using X-ray photoelectron spectroscopy (XPS, Fig. 2g) provided detailed information on the compositions and electronic states of the two MOFs. The Zn 2*p* spectrum (Fig. 2h) showed peaks at 1021.96 eV and 1044.90 eV, corresponding to Zn<sup>2+</sup> 2*p*<sub>3/2</sub> and 2*p*<sub>1/2</sub> states, respectively. Similarly, the Ni 2*p* spectrum (Fig. 2i) featured peaks at 856.24 eV and 873.88 eV for Ni<sup>2+</sup> 2*p*<sub>3/2</sub>, and 862.12 eV and 879.79 eV for Ni<sup>2+</sup> 2*p*<sub>1/2</sub>, confirming the oxidation state of the metal centers. The C 1*s* spectrum (Supplementary Fig. 3a) revealed peaks at 284.38 eV and 285.78 eV, corresponding to C-C/C=C and C-N/C=N bonds, respectively, while the N 1*s* spectrum (Supplementary Fig. 3b) showed peaks at 399.08 eV and 399.68 eV,

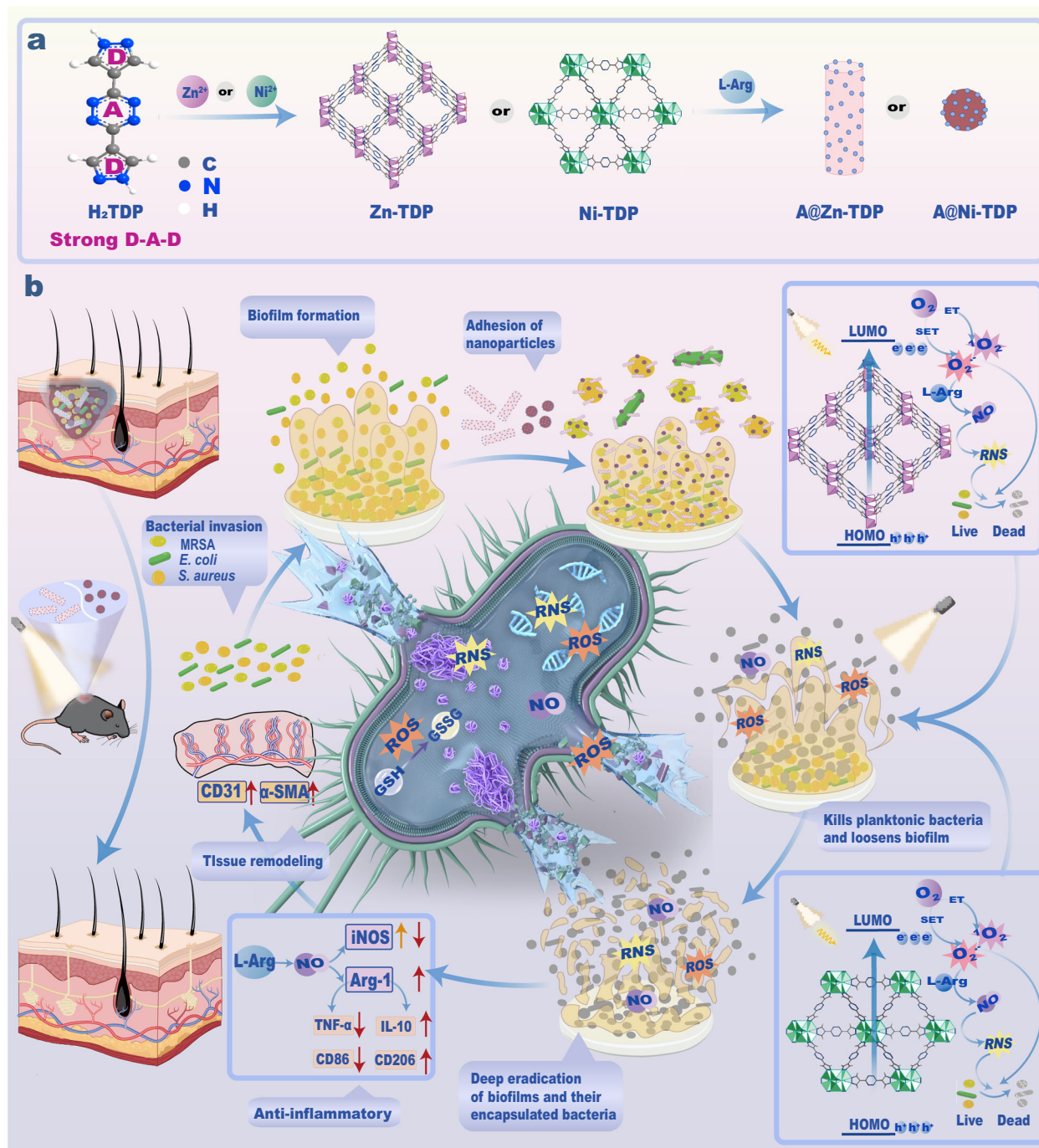


**Fig. 1 | Schematic overview of the tetrazine-enhanced MOF platform for anti-bacterial therapy.** **a** Schematic illustration of the preparation of A@Zn-TDP and A@Ni-TDP composites. **b** Mechanism of action depicting photodynamic

antibacterial activity, biofilm eradication, and promotion of wound healing. The mouse illustration was adapted from Adult Mouse by Yunan Chen, available on SciDraw ([scidraw.io](http://scidraw.io)) under a CC BY 4.0 license.

corresponding to Zn-N and N-N/N=N bonds. Similar XPS profiles were observed for Ni-TDP. These findings highlight that the incorporation of tetrazine rings into the MOF structures preserves their integrity while offering promising possibilities for designing robust, tetrazine-based MOFs.

To explore the photochemical properties of Zn-TDP and Ni-TDP, we first measured the maximum emission wavelength and UV-vis absorption of H<sub>2</sub>TDP and H<sub>2</sub>BDP in DMF solution (Supplementary Fig. 4). H<sub>2</sub>TDP showed a strong emission peak at 586 nm upon excitation at 365 nm and a distinct absorption peak at 538 nm in its UV-vis spectrum. In contrast, H<sub>2</sub>BDP displayed no visible light absorption,

highlighting the markedly different electronic properties of H<sub>2</sub>TDP. We then recorded the UV-vis diffuse reflectance spectra (DRS) of Zn-TDP and Ni-TDP (Fig. 3a). Both MOFs exhibited prominent absorption bands at around 550 nm, similar to the free H<sub>2</sub>TDP ligand. Ni-TDP also displayed a broad absorption peak at around 630 nm, which corresponds to the ligand field transitions of Ni<sup>2+</sup>, a feature also observed in its analog Ni-BDP<sup>42</sup>. The electronic structures of Zn-TDP and Ni-TDP were evaluated by combining Mott–Schottky analysis (Supplementary Fig. 5) and Tauc plots (Supplementary Fig. 6), with the calculated HOMO and LUMO energy levels summarized in Fig. 3b. Both MOFs exhibited markedly reduced band gaps—2.11 eV for Zn-TDP and 1.64 eV

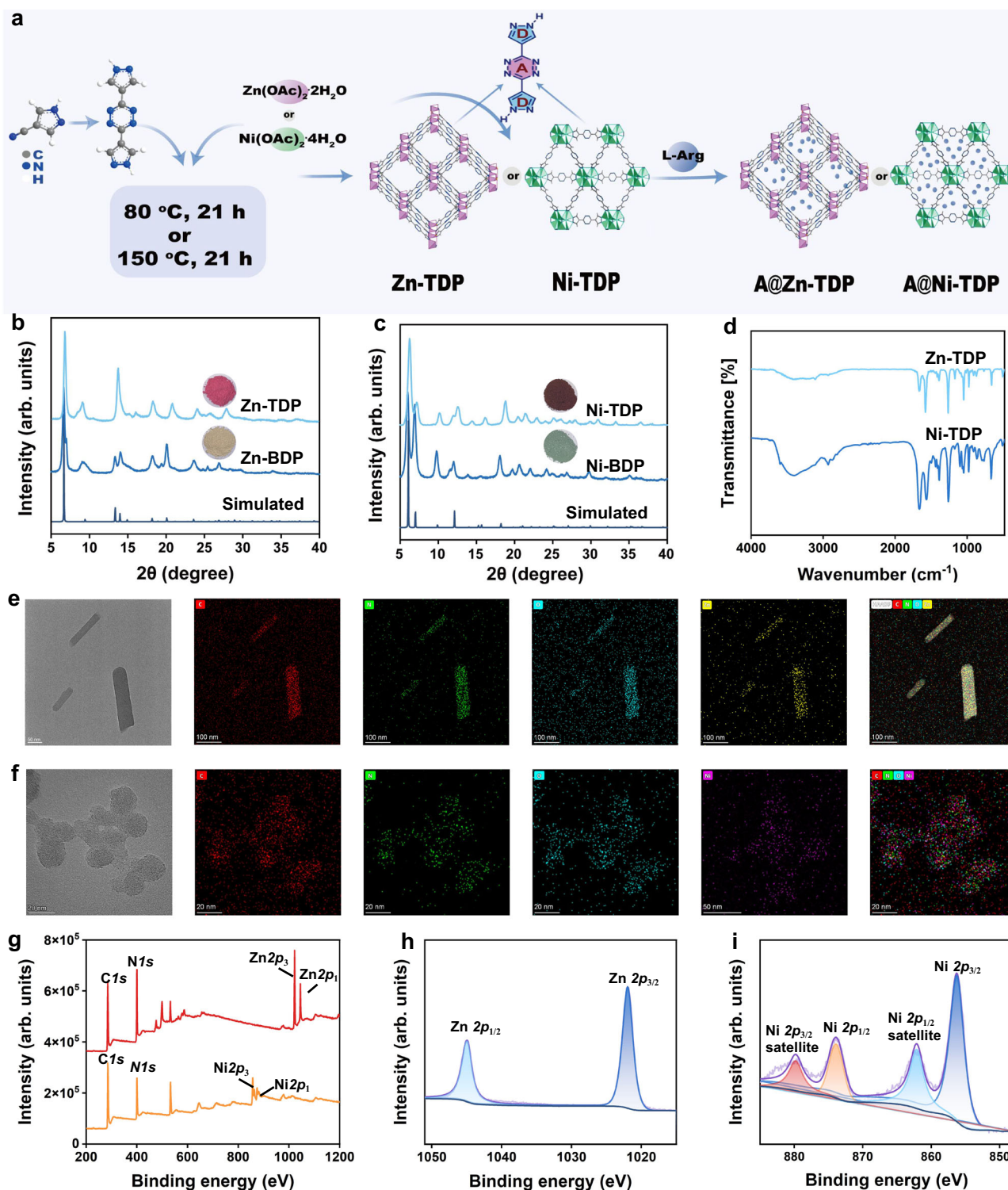


**Fig. 2 | Characterizations of Zn-TDP and Ni-TDP.** **a** Synthesis of Zn-TDP, Ni-TDP, A@Zn-TDP, and A@Ni-TDP. **b** PXRD patterns of Zn-BDP and Zn-TDP. **c** PXRD patterns of Ni-BDP and Ni-TDP. **d** FT-IR spectra of Zn-TDP and Ni-TDP. **e** TEM image of Zn-TDP and the EDS elemental mapping. **f** TEM image of Ni-TDP and the EDS

elemental mapping. Images from three independent samples were acquired, and a representative example is shown in (e) and (f). **g** XPS full spectrum of Zn-TDP and Ni-TDP. **h** Zn 2*p* spectrum of Zn-TDP. **i** Ni 2*p* spectrum of Ni-TDP. Source data are provided as a Source Data file.

for Ni-TDP—compared to their benzene-based analogues, Zn-BDP (3.73 eV) and Ni-BDP (3.45 eV). The pronounced narrowing of the band gap demonstrates that incorporating tetrazine as a strong electron acceptor within the D–A–D framework effectively enhances charge separation compared with the weaker benzene-based system. Consequently, the materials exhibit improved electron transfer to molecular

oxygen, thereby facilitating its reduction ( $O_2/O_2^-$  redox potential at  $-0.33\text{ V}$ )<sup>43</sup>. Collectively, these photochemical and electronic enhancements are expected to yield superior photocatalytic ROS generation, enabling highly efficient antibacterial activity and underscoring the potential of Zn-TDP and Ni-TDP as promising platforms for advanced light-driven antimicrobial therapies.

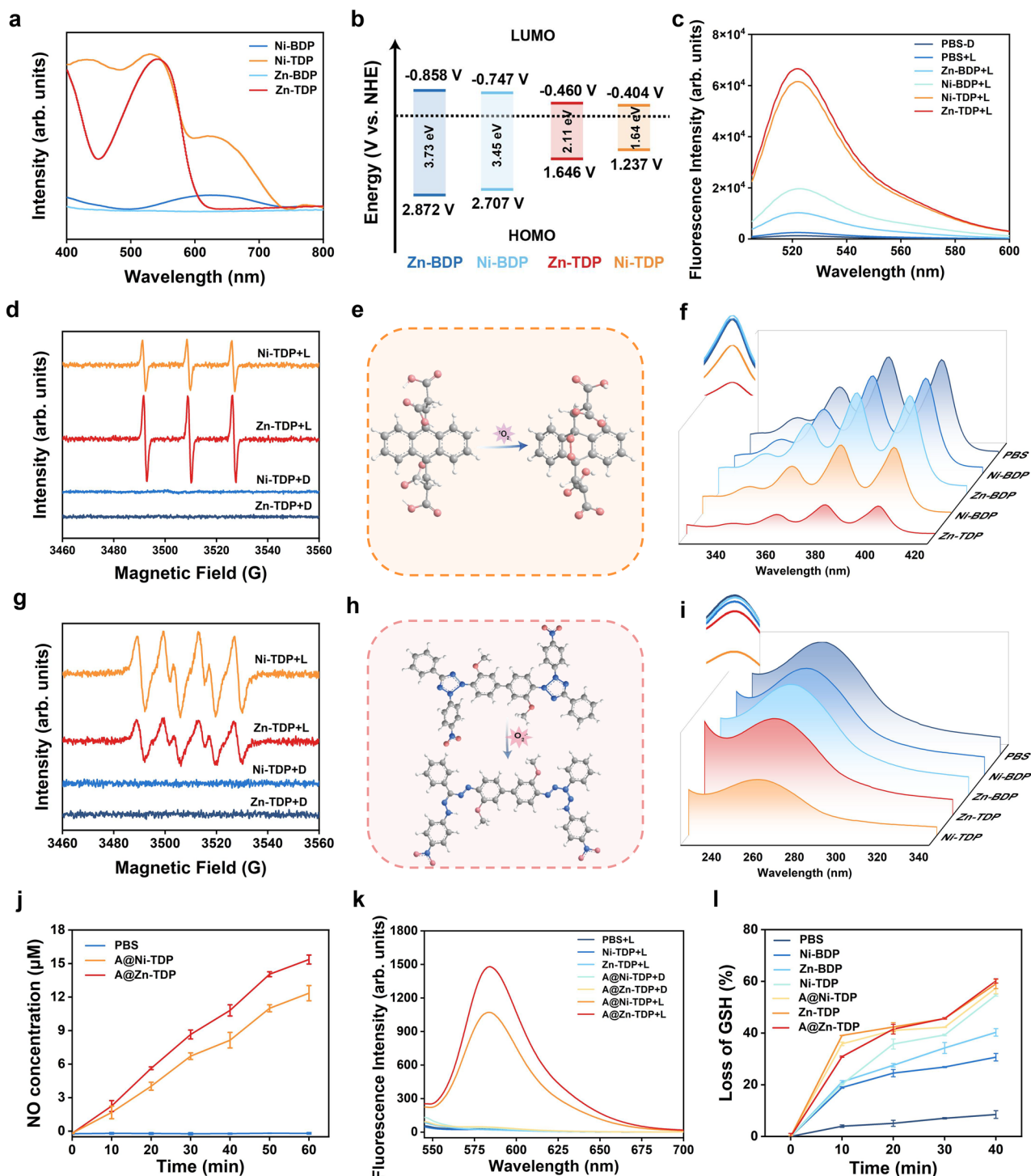


**Fig. 3 | Assessment of photocatalytic performance, NO and ONOO<sup>-</sup> release effects.** **a** UV-vis DRS of Zn-BDP, Zn-TDP, Ni-BDP and Ni-TDP. **b** Schematic diagrams of the optical band gap of Zn-BDP, Zn-TDP, Ni-BDP and Ni-TDP. **c** UV-vis absorption spectra of DCFH in different samples under irradiation (420–780 nm, 150 mW/cm<sup>2</sup>, 5 min). **d** EPR spectra of Zn-TDP and Ni-TDP with TEMP under irradiation. **e** Consumption mechanism and **f** absorption curves of ABDA at wavelengths from 325 to 425 nm. **g** EPR spectra of Zn-TDP and Ni-TDP with DMPO.

**h** Consumption mechanism and **i** absorption curves of NBT at wavelengths from 225 to 325 nm. **j** NO release from A@Zn-TDP and A@Ni-TDP ( $n = 3$  independent samples per group, data are presented as mean  $\pm$  SD). **k** ONOO<sup>-</sup> generation for A@Zn-TDP and A@Ni-TDP. **l** Irradiation time-dependent plot of the reduction rate of GSH ( $n = 3$  independent samples per group, data are presented as mean  $\pm$  SD). D for darkness, L for light. Source data are provided as a Source Data file.

### Generation of ROS

Building on the optimized electronic band structures of Zn-TDP and Ni-TDP, we evaluated the ROS generation capabilities of Zn-TDP and Ni-TDP under visible-light irradiation using 2',7'-dichlorodihydrofluorescein diacetate (DCFH-DA) as a fluorescent probe (Fig. 3c). For the reference

MOFs, Zn-BDP and Ni-BDP, only a slight increase in fluorescence intensity at 525 nm was observed after 5 minutes of light exposure, indicating limited ROS production. In contrast, both Zn-TDP and Ni-TDP displayed a significant increase in fluorescence intensity, indicating considerably higher ROS generation. Among the two, Zn-TDP exhibited the greatest

increase, which may be due to the shorter Zn–Zn distance, facilitating long-range energy/electron transfer, thus enhancing photocatalytic efficiency<sup>44</sup>.

To identify the types of ROS generated, electron paramagnetic resonance (EPR) spectroscopy was conducted (Fig. 3d, g). Using 2,2,6,6-tetramethylpiperidine (TEMP) as a trapping agent, both Zn-TDP and Ni-TDP showed strong signals corresponding to TEMP-<sup>1</sup>O<sub>2</sub> adducts, confirming the presence of <sup>1</sup>O<sub>2</sub>. Similarly, when 5,5-dimethyl-1-pyrroline-N-oxide (DMPO) was used as a trap for superoxide radicals (<sup>•</sup>O<sub>2</sub><sup>-</sup>), distinct EPR signals for DMPO-<sup>•</sup>O<sub>2</sub><sup>-</sup> adducts were observed in both MOFs, verifying the formation of <sup>•</sup>O<sub>2</sub><sup>-</sup>. To further differentiate the generation profiles of <sup>1</sup>O<sub>2</sub> and <sup>•</sup>O<sub>2</sub><sup>-</sup>, additional ROS probes, including 9,10-anthracenediylbis(methylene)dimalonic acid (ABDA) and nitro blue tetrazolium chloride (NBT), were employed to differentiate between <sup>1</sup>O<sub>2</sub> and <sup>•</sup>O<sub>2</sub><sup>-</sup> generation. Under irradiation, the absorbance of ABDA at 400 nm (Fig. 3e, f) decreased significantly for Zn-TDP, while the decrease was more gradual for Ni-TDP. Conversely, a more rapid decline in NBT absorbance at 259 nm was observed for Ni-TDP compared to Zn-TDP (Fig. 3h, i). These findings suggest that Zn-TDP predominantly generates <sup>1</sup>O<sub>2</sub> via an energy transfer mechanism, whereas Ni-TDP favors the production of <sup>•</sup>O<sub>2</sub><sup>-</sup> through an electron transfer pathway. It is well documented that <sup>1</sup>O<sub>2</sub> possesses a stronger oxidative capacity and shorter diffusion distance compared to <sup>•</sup>O<sub>2</sub><sup>-</sup>, which may partly explain the superior ability of Zn-TDP in oxidizing DCFH as observed in earlier assays. The higher oxidative potential and cytotoxic efficiency of <sup>1</sup>O<sub>2</sub> likely contribute to more effective microbial inactivation, suggesting that Zn-TDP may exhibit enhanced photodynamic antibacterial activity over Ni-TDP.

### Loading of therapeutic molecule and release of active substances

Capitalizing on their stable microporous structures, we incorporated L-Arg into Zn-TDP and Ni-TDP to broaden the therapeutic functionality of these nanomaterials. As a natural NO donor with high biocompatibility, L-Arg not only enables controllable NO release via both enzymatic catalysis by nitric oxide synthase and oxidative degradation of its guanidine group but also facilitates immunomodulatory effects<sup>45</sup>. L-Arg was incorporated via direct diffusion, yielding the composites A@Zn-TDP and A@Ni-TDP. Structural characterizations by PXRD, FTIR, and TEM (Supplementary Figs. 1, 7, and 8) confirmed that both composites retained the structural integrity and morphology of the parent MOFs. Thermogravimetric analysis (TGA, Supplementary Fig. 9) showed significant weight losses between 100–200 °C for both A@Zn-TDP and A@Ni-TDP, attributed to decomposition of incorporated L-Arg and evaporation of residual solvents. Quantitative analysis determined L-Arg loadings of 24.75 ± 1.13 wt% for Zn-TDP and 18.97 ± 1.31 wt% for Ni-TDP (Supplementary Fig. 10), with the variation likely due to differences in surface chemistry, pore accessibility, and metal–ligand interactions between the two frameworks. Dynamic light scattering (DLS) measurements revealed hydrated diameters of 329.4 ± 2.2 nm for Zn-TDP and 247.0 ± 0.6 nm for Ni-TDP (Supplementary Fig. 11), with particle sizes decreasing to 268.6 ± 0.8 nm (A@Zn-TDP) and 166.2 ± 0.9 nm (A@Ni-TDP) upon L-Arg loading, suggesting that surface modification with L-Arg improves hydrophilicity and dispersibility. Sizes remained in the ranges after five days in PBS (Supplementary Fig. 12), confirming high physiological stability. This was further supported by ICP-MS analysis (Supplementary Table 2), which detected minimal Zn<sup>2+</sup> or Ni<sup>2+</sup> ion leaching (< 0.7% in all cases). The exceptionally low metal release underscores the stability of the coordinative bonds within these MOFs, which is essential for minimizing cytotoxicity and enabling prolonged therapeutic applications—such as nitric-oxide-enhanced photodynamic therapy and immunomodulation in chronic wound environments—thereby highlighting the structural robustness and biosafety potential of the composites.

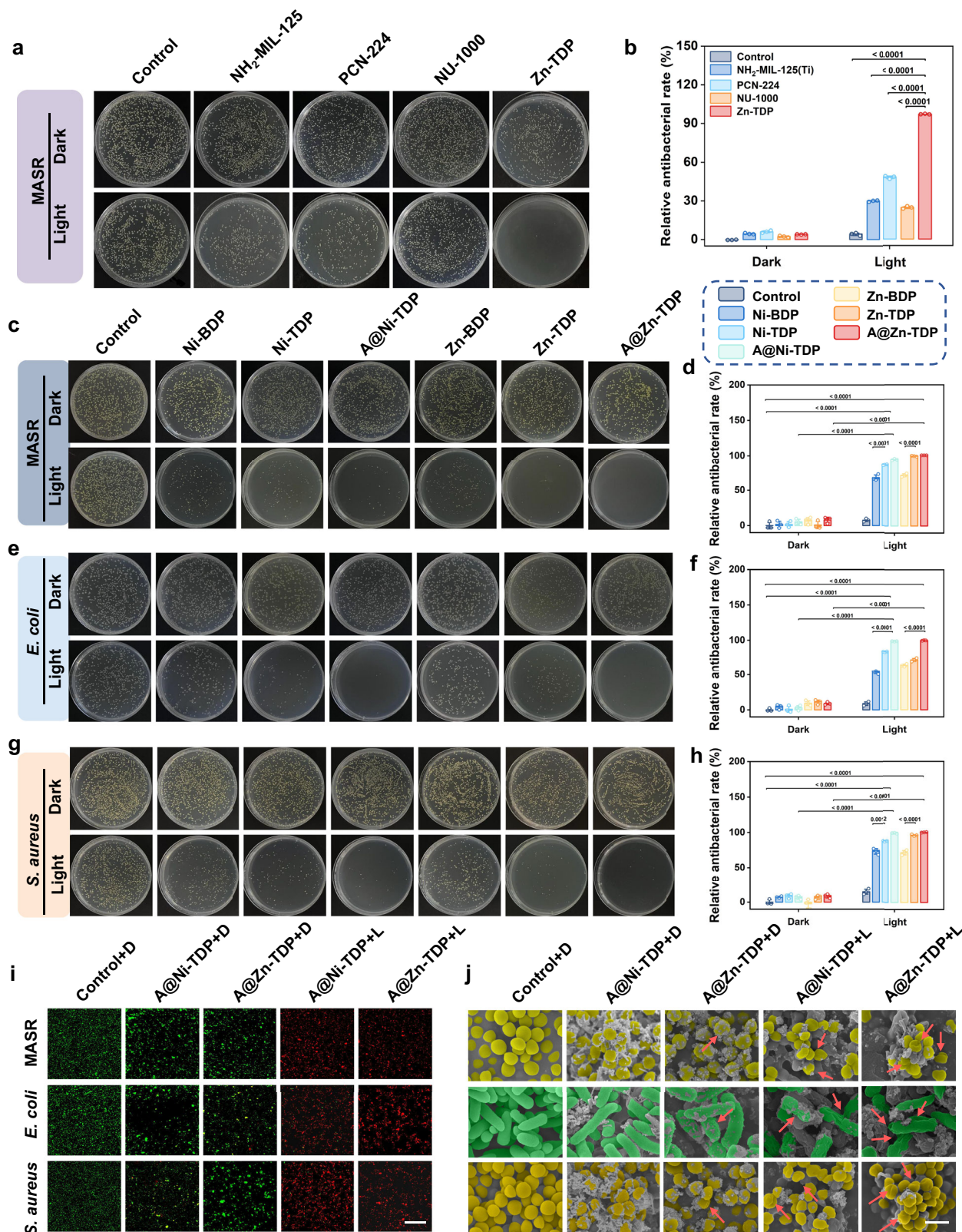
Under light irradiation, ROS generated by the tetrazine-enhanced frameworks oxidized the guanidine group of L-Arg, triggering controlled NO release, as confirmed by Griess assays (Fig. 3j). Negligible NO release was observed in darkness, while NO production increased progressively with irradiation time, reaching 15.36 ± 0.41 μM for A@Zn-TDP and 12.36 ± 0.68 μM for A@Ni-TDP after 60 minutes. The release of NO was dependent on both light intensity and material concentration (Supplementary Fig. 13). The observed increase in NO production with higher light intensity and catalyst loading indicates a positive correlation between NO release and light-driven ROS generation, suggesting that the system operates under photon- and catalyst-limited conditions rather than being constrained by intrinsic reaction kinetics. Specifically, stronger light irradiation enhances the generation of photoexcited charge carriers, thereby accelerating ROS formation and subsequent NO production, while higher catalyst concentrations provide additional active sites and improve light absorption. The absence of saturation within the tested range implies that charge separation and transfer remain highly efficient, with minimal recombination losses. These results underscore the effectiveness of the tetrazine-based MOF composites and suggest that further optimization of reaction conditions could further enhance their photodynamic performance.

Importantly, the combined generation of ROS and NO facilitated the formation of ONOO<sup>-</sup>. Compared to controls—Zn-TDP and Ni-TDP under light (without L-Arg) and A@Zn-TDP and A@Ni-TDP in darkness—the irradiated A@Zn-TDP and A@Ni-TDP composites exhibited significantly enhanced ONOO<sup>-</sup> fluorescence<sup>46</sup> signals (λ<sub>ex</sub> = 535 nm, λ<sub>em</sub> = 584 nm, Fig. 3k), verifying the production of peroxynitrite, a highly reactive RNS critical for effective antibacterial activity. This stepwise, dual-responsive system offers several intrinsic advantages for antibacterial applications. It allows for precisely controllable, light-triggered release of bioactive species, minimizing off-target effects and enhancing safety. In the initial phase, light-induced ROS rapidly kills bacteria and disrupts the protective biofilm matrix, creating channels for deeper penetration. Subsequently, ROS-triggered NO release and the subsequent formation of RNS infiltrate the biofilm interior, enabling thorough eradication of residual bacteria that are often resistant to conventional treatments. This sequential mechanism not only maximizes bactericidal efficiency but also mitigates the risk of bacterial regrowth, highlighting the potential of the tetrazine-enhanced MOF composites as robust and versatile platforms for treating persistent biofilm-associated infections.

Given the high concentration of reducing agents, such as glutathione (GSH), in bacterial environments to counteract oxidative stress, we further explored the GSH-scavenging capabilities of A@Zn-TDP and A@Ni-TDP using 5,5'-dithiobis(2-nitrobenzoic acid) (DTNB) as a detection probe (Fig. 3l and Supplementary Fig. 14). We observed that both Zn-TDP and Ni-TDP, along with their L-Arg-loaded counterparts, exhibited enhanced GSH oxidation under visible light excitation. This resulted in a dramatic reduction in the characteristic yellow color of the DTNB solution, indicating effective GSH scavenging. The scavenging performance can be ascribed to the robust and continuous generation of reactive species (ROS, NO, and subsequently RNS) from the tetrazine-enhanced D–A–D MOF composites under photo-irradiation, which effectively overwhelms the local antioxidant defense system. Unlike single-mode ROS generation, the stepwise production of multiple reactive species can not only cause direct oxidative damage to bacterial membranes, proteins, and nucleic acids but also disrupt intracellular redox homeostasis by depleting endogenous reducing agents such as GSH.

### In vitro antibacterial activity

Building on the demonstrated high efficiency of photocatalytic ROS generation, we evaluated the broad-spectrum antimicrobial activity of these tetrazine-based MOFs and their L-Arg-loaded composites against clinically relevant wound pathogens, including *S. aureus*, *E. coli*, and



MRSA. Using MRSA as a representative model, colony counting assays (Fig. 4c, d) showed that Zn-TDP (25  $\mu\text{g}/\text{mL}$ ) achieved a high bactericidal rate of  $98.85 \pm 0.58\%$  within just 15 minutes of visible-light irradiation, significantly outperforming its benzene-based analogue Zn-BDP ( $71.84 \pm 2.36\%$ ). Notably, Zn-TDP also exhibited superior antibacterial activity compared to widely studied photosensitizing MOFs (Fig. 4a, b), including PCN-224 ( $48.02 \pm 1.17\%$ ), NH<sub>2</sub>-MIL-125 ( $29.83 \pm 0.52\%$ ), and

NU-1000 ( $24.60 \pm 0.99\%$ ). The exceptional photodynamic antibacterial performance of Zn-TDP can be primarily attributed to the strong electron-withdrawing capacity of the tetrazine unit and the enhanced charge separation efficiency imparted by the D–A–D structure. Such efficient photophysical processes translate into a substantial enhancement in the yield of cytotoxic ROS as well as photodynamic antibacterial efficacy. Importantly, the robust and tunable

**Fig. 4 | In vitro evaluation of antibacterial activity against planktonic bacteria.** Plate colony patterns (a) and quantitative analysis (b) comparing the anti-MRSA efficacy of the tetrazine-enhanced MOF Zn-TDP with other conventional photosensitive MOFs (25 µg/mL) ( $n = 3$  independent biological replicates, data are presented as mean  $\pm$  SD). Colony-forming unit (CFU) counts and antibacterial rates of MRSA (25 µg/mL, light exposure 15 min for Zn-TDP and A@Zn-TDP, 250 µg/mL, light exposure 30 min for Ni-TDP and A@Ni-TDP) (c), *E. coli* (50 µg/mL, light exposure 15 min for Zn-TDP and A@Zn-TDP, 200 µg/mL, light exposure 30 min for Ni-TDP and A@Ni-TDP) (e), and *S. aureus* (25 µg/mL, light exposure 15 min for Zn-TDP and A@Zn-TDP, 200 µg/mL, light exposure 30 min for Ni-TDP and A@Ni-TDP) (g) under different treatment conditions, with corresponding quantitative results shown in (d), (f), and (h), respectively ( $n = 3$  independent biological replicates, data are

presented as mean  $\pm$  SD). (The colors of each group in (d), (f) and (h) correspond to the colors labeled above them.) i SYTO-9/PI bacterial live (green fluorescence)/dead (red fluorescence) staining images of MRSA, *E. coli* and *S. aureus* after different treatments, scale bars = 200 µm. j SEM images illustrating the changes on the morphology of bacteria, scale bar = 1 µm, (false color applied). Images from three independent biological replicates were acquired, and a representative example is shown in (i) and (j). Control denotes the group received an equal volume of physiological saline followed by either dark or light exposure, whereas Control+D indicates administration of an equal volume of physiological saline followed by dark exposure, D for darkness, L for light. Statistical significance was determined by one-way ANOVA followed by Tukey's post hoc test for multiple comparisons (b, d, f, and h). Source data are provided as a Source Data file.

photodynamic activity of Zn-TDP establishes a versatile foundation for constructing multi-component therapeutic systems. By integrating ROS generation with complementary bactericidal mechanisms—such as nitric oxide release—these MOFs can achieve a combined multi-hit antibacterial effect. Such an approach not only enhances pathogen eradication but also diminishes the likelihood of bacterial resistance development, particularly in challenging contexts such as biofilm-associated and chronic infections.

Upon L-Arg loading, the resulting composites (A@Zn-TDP and A@Ni-TDP) exhibited improved antibacterial performance (Fig. 4c, d). Their positive surface charge facilitated strong adhesion to negatively charged bacterial membranes (Supplementary Fig. 17), reducing the ROS diffusion distance to maximize bactericidal effects. SEM imaging confirmed this enhanced bacterial adhesion (Fig. 4j). A@Zn-TDP achieved near-complete eradication (> 99.99%) of MRSA, a notable outcome that may result from the combined interplay of improved bacterial membrane targeting, oxidation-triggered NO release, and the subsequent formation of highly toxic RNS.

For Ni-based MOFs, Ni-BDP (Fig. 4c, d) showed limited antibacterial efficacy ( $67.85 \pm 4.34\%$ ) even at higher concentrations (250 µg/mL), while Ni-TDP and A@Ni-TDP achieved bactericidal rates of  $86.52 \pm 0.91\%$  and  $95.95 \pm 0.96\%$ , respectively. Interestingly, A@Zn-TDP demonstrated superior bactericidal efficiency at significantly lower concentrations and shorter irradiation times compared to A@Ni-TDP, likely due to its higher generation of ROS, particularly  $^1O_2$ , which is known for potent and rapid bacterial membrane disruption<sup>33</sup>. Crucially, this potent bactericidal effect was achieved at a dosage of only 25 µg/mL, highlighting a significant improvement over conventional PDT that often require substantially higher concentrations to achieve comparable efficacy. By reducing the dosage threshold, A@Zn-TDP not only minimizes potential cytotoxicity to surrounding healthy tissues but also enhances therapeutic safety and clinical applicability. Control experiments using individual components ( $H_2TDP$ ,  $Zn(OAc)_2$ ,  $Ni(OAc)_2$ , L-Arg) or NO donors alone ( $NaNO_2$ <sup>47</sup>, GSNO<sup>48</sup>) showed negligible antibacterial activity (Supplementary Figs. 18 and 21), confirming that the observed effects arise from the combined photodynamic, NO, and RNS actions of the D-A-D photosensitive MOF composites rather than any single component.

Antimicrobial assessments against *E. coli* and *S. aureus* further validated the broad-spectrum efficacy of Zn-TDP, A@Zn-TDP, Ni-TDP, and A@Ni-TDP, which exhibited bactericidal trends consistent with those observed against MRSA (Fig. 4e–h, Supplementary Figs. 15–16, and Supplementary Figs. 19–21). These results highlight the potent activity of these materials against both Gram-positive and Gram-negative pathogens, underscoring their robust and broad-spectrum antimicrobial potential. Optimal antibacterial conditions were identified as 25 µg/mL, 15 min, and 150 mW/cm<sup>2</sup> for A@Zn-TDP, and 250 µg/mL, 30 min, and 150 mW/cm<sup>2</sup> for A@Ni-TDP (Supplementary Figs. 22–29), and these parameters were used for subsequent experiments. Bacterial growth curves (Supplementary Fig. 30) under these conditions further showed effective inhibition of all three strains tested.

To visualize bacterial viability, LIVE/DEAD staining (Fig. 4i and Supplementary Fig. 31) was used. In all tested strains (*E. coli*, *S. aureus*, and MRSA), the control and dark-treated groups predominantly showed green fluorescence, indicating high bacterial viability. In contrast, A@Zn-TDP and A@Ni-TDP treatments under optimal conditions led to a strong red fluorescence, signifying extensive bacterial cell death. Treated bacteria also aggregated around the MOFs, suggesting effective trapping and interaction. SEM images (Fig. 4j) confirmed these results. While untreated bacteria had smooth surfaces and intact structures, A@Zn-TDP + L and A@Ni-TDP + L-treated cells displayed severe morphological damage, including wrinkling, concavity, and cracking (pink arrows in Fig. 4j), consistent with the attack of reactive species on membrane integrity and intracellular components.

### In vitro anti-biofilm ability

The tetrazine-enhanced MOFs and their L-Arg-loaded composites exhibited notable efficacy against recalcitrant biofilm infections. Semi-quantitative crystal violet staining (Fig. 5a, c) revealed that A@Zn-TDP under light irradiation (A@Zn-TDP + L) dramatically reduced MRSA biofilm biomass ( $OD_{590} = 0.97 \pm 0.08$ ) compared to untreated controls ( $OD_{590} = 3.67 \pm 0.03$ ) and dark conditions. A@Ni-TDP + L also reduced biofilm formation ( $OD_{590} = 1.64 \pm 0.09$ ), albeit to a lesser extent. Similar trends were observed for *E. coli* and *S. aureus* biofilms, confirming the broad applicability of this approach. Colony enumeration assays (Fig. 5b, d) further confirmed these findings, showing exceptional bactericidal activity with only  $0.97 \pm 0.39\%$  MRSA survival after A@Zn-TDP + L treatment, compared to  $21.04 \pm 1.77\%$  survival with A@Ni-TDP + L. This superior eradication efficacy of A@Zn-TDP was consistently observed across other tested pathogens, underscoring its potential as a leading candidate for biofilm eradication.

SYTO-9/PI staining coupled with 3D fluorescence imaging (Fig. 5e) visualized extensive biofilm disruption and loss of bacterial viability following treatment with A@Zn-TDP + L and A@Ni-TDP + L, while control and dark-treated groups retained almost intact biofilm structures. Notably, A@Zn-TDP + L treatment resulted in dominant PI (red) fluorescence, indicating widespread bacterial membrane damage. Flow cytometry analysis further substantiated these findings, revealing a markedly increased proportion of PI-positive cells in the treated groups (Fig. 5f and Supplementary Fig. 32). This outcome is consistent with the hypothesis that excessive ROS/RNS generation induces lipid and protein peroxidation, thereby compromising membrane integrity and leading to loss of cellular viability. SEM images (Fig. 5g) further illustrated the profound anti-biofilm effects, revealing complete structural disintegration of treated biofilms, characterized by cell wrinkling, inward concavity, and extensive surface damage. In contrast, untreated controls maintained dense, intact biofilm matrices.

In summary, these findings demonstrate that the tetrazine-enhanced MOF composites—particularly A@Zn-TDP—exhibit potent antibiofilm efficacy. This may benefit from the dual-responsive pathway that enables the stepwise release of ROS, NO, and RNS. Mechanistically, the composites initially adhere to the biofilm periphery, where photoactivation triggers a rapid burst of ROS. These highly

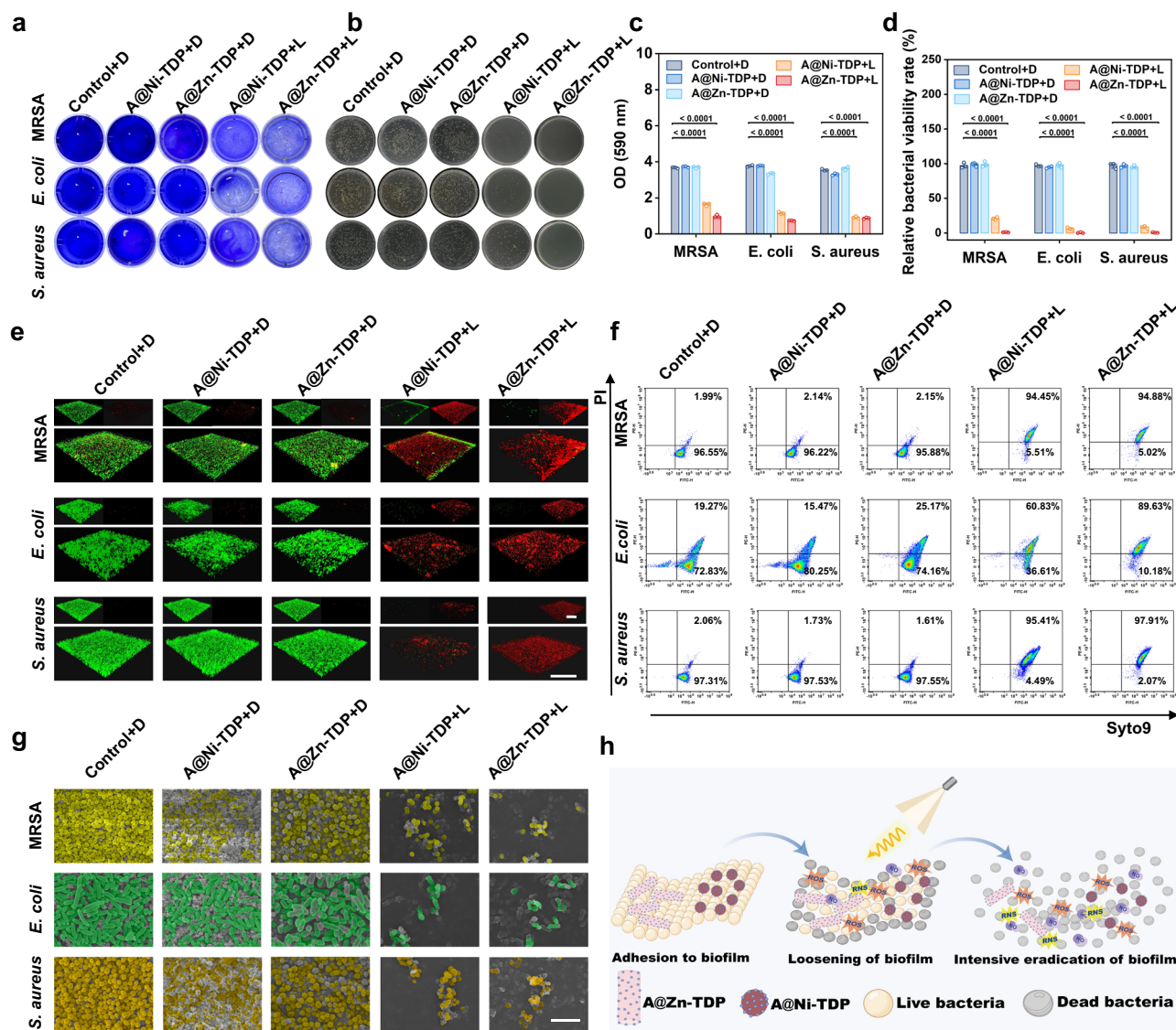


**Fig. 5 | Evaluation of in vitro anti-biofilm activity.** MRSA, *E. coli* and *S. aureus* biofilms treated with saline, A@Zn-TDP and A@Ni-TDP under dark or irradiation, crystal violet staining condition images (a), photos of surviving colonies in a biofilm (b), UV absorption values of crystal violet at 590 nm (c) ( $n = 3$  independent biological replicates, data are presented as mean  $\pm$  SD), and quantitative analysis of residual bacteria (d) ( $n = 3$  independent biological replicates, data are presented as mean  $\pm$  SD). e 3D reconstructed fluorescence images of MRSA, *E. coli* and *S. aureus* biofilms stained with SYTO 9/PI (scale bar = 100  $\mu$ m). f Flow cytometry results showing bacterial live/dead staining of MRSA, *E. coli* and *S. aureus* biofilms after

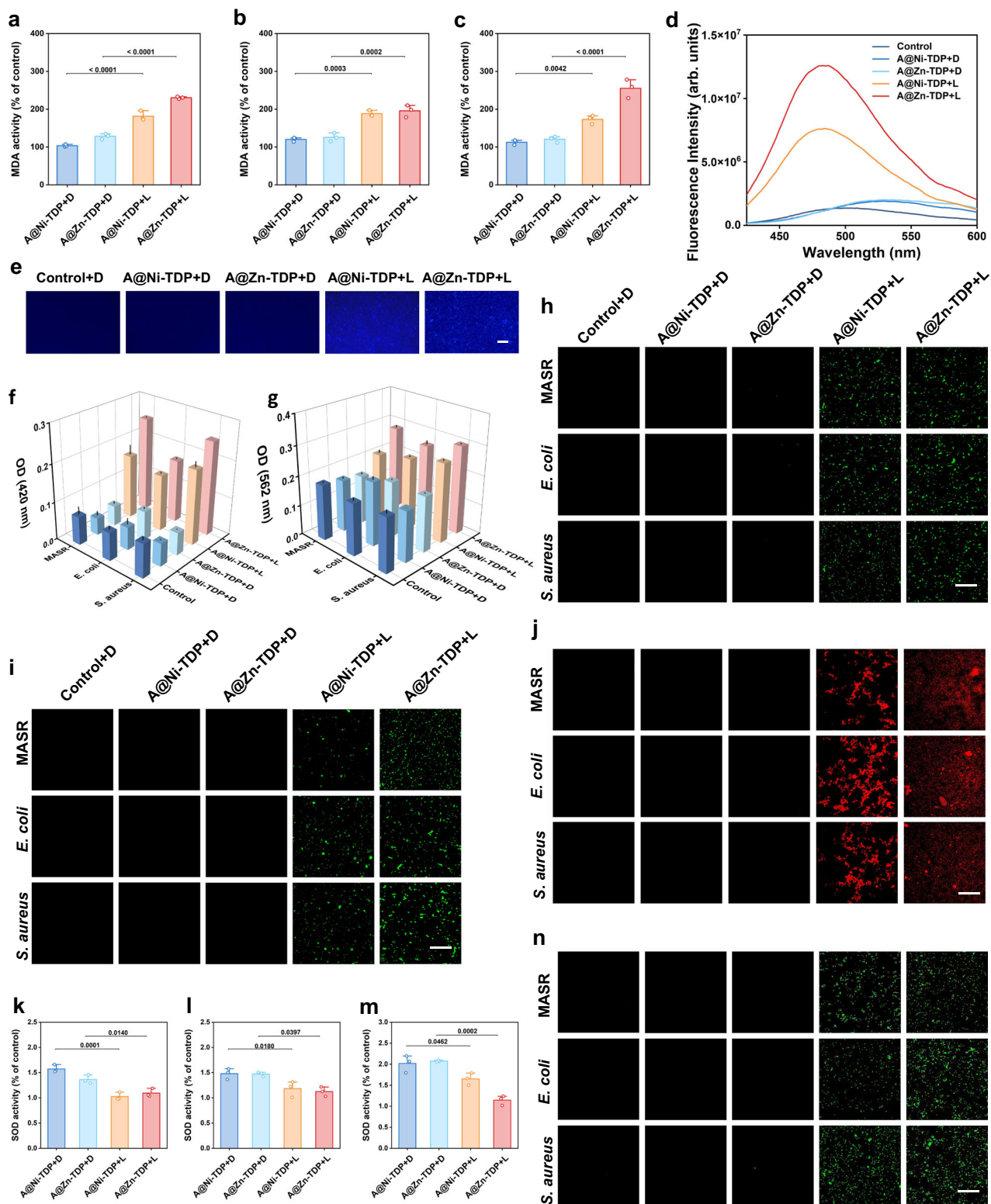
different treatments. g) SEM images of the biofilm (scale bar = 5  $\mu$ m, false color applied). Images from three independent biological replicates were acquired, and a representative example is shown in (e) and (g). h Schematic illustration of biofilm elimination by A@Zn-TDP and A@Ni-TDP. Control+D indicates administration of an equal volume of physiological saline followed by dark exposure. D for darkness, L for light. Statistical significance was determined by one-way ANOVA followed by Tukey's post hoc test for multiple comparisons (c, d). Source data are provided as a Source Data file.

cytotoxic species eradicate superficial bacteria and compromise the EPS matrix, thereby creating channels that facilitate the deeper penetration of subsequent reactive intermediates. Concurrently, ROS-mediated oxidation of L-Arg drives substantial NO release. As a diffusible gaseous signaling molecule, NO readily permeates into the deeper layers of the biofilm, where it further disrupts bacterial metabolism and viability. The process is amplified by the secondary formation of RNS, which exert persistent peroxidative stress, ensuring comprehensive biofilm eradication (Fig. 5h).

#### Antibacterial mechanism

Given the exceptional antibacterial and anti-biofilm performance of A@Zn-TDP and A@Ni-TDP, we investigated their underlying mechanisms. Assessment of membrane peroxidative damage through malondialdehyde (MDA) quantification revealed that under irradiation

(Fig. 6a–c), A@Zn-TDP and A@Ni-TDP increased MDA levels in MRSA by  $130.28 \pm 2.93\%$  and  $81.34 \pm 12.82\%$  versus dark controls, respectively, reflecting severe membrane lipid peroxidation induced by reactive species. Analogous trends in *E. coli* and *S. aureus* confirmed widespread and irreversible membrane oxidative damage. Concurrently, membrane permeability assays using 8-anilino-1-naphthalenesulfonic acid (ANS) and o-nitrophenyl- $\beta$ -D-galactopyranoside (ONPG) demonstrated: enhanced outer membrane permeability evidenced by increased ANS fluorescence in *E. coli* (Fig. 6d, e), and elevated inner membrane permeability verified by elevated ONPG absorbance at 420 nm in all strains (Fig. 6f). Furthermore, the apparent efflux of contents from MRSA, *E. coli* and *S. aureus* cells after A@Zn-TDP + L and A@Ni-TDP + L treatments in the protein leakage assay emphasized the severe disruption of the bacterial membrane (Fig. 6g), suggesting a loss of membrane selectivity and cytosol leakage.



We next examined intracellular reactive species. Light-activated ROS generation was observed through intense green fluorescence (DCFH-DA) across all strains (Fig. 6h), while DAF-FM-DA staining confirmed substantial NO production (Fig. 6i). Moreover, corresponding RNS probes revealed significant red fluorescence (Fig. 6j). These collectively provide evidence for the formation of reactive species (ROS, NO, and RNS) within bacterial cells. This oxidative burst disrupted the bacterial redox homeostasis, pushing cells into a state of severe

oxidative stress. Therefore, we measured the activities of key oxidoreductases, including superoxide dismutase (SOD), catalase (CAT), and NADPH oxidase (NOX) (Fig. 6k–m, and Supplementary Figs. 33–34). SOD activity increased in all bacterial strains after dark or light treatment with the material; however, the activity was higher in dark-treated samples, suggesting a compensatory upregulation mechanism in response to the initial stress induced by the A@Zn-TDP or A@Ni-TDP composites. Crucially, after irradiation, the bacterial antioxidant

**Fig. 6 | Exploration of antimicrobial mechanisms.** Levels of the lipid peroxidation product MDA in MRSA (a), *E. coli* (b) and *S. aureus* (c) ( $n = 3$  independent biological replicates, data are presented as mean  $\pm$  SD). Fluorescence intensities indicating changes of outer membrane permeation of *E. coli* (d), and blue fluorescent images (e) with ANS ( $\lambda_{\text{ex}} = 380$  nm,  $\lambda_{\text{em}} = 450 - 600$  nm). ONPG assay evaluating the permeability of the bacterial inner membrane in MRSA, *E. coli*, and *S. aureus* after various treatments (f), and the corresponding protein leakage (g) ( $n = 3$  independent biological replicates, data are presented as mean  $\pm$  SD). h ROS in the MRSA, *E. coli* and *S. aureus* induced by different samples under dark or irradiation, (scale bar = 200  $\mu\text{m}$ , green fluorescence indicates generation of ROS in the interior of bacteria). i NO in the MRSA, *E. coli* and *S. aureus* after different treatments, (scale bar = 200  $\mu\text{m}$ , green fluorescence indicates NO in the bacteria). j ONOO<sup>-</sup> in the MRSA, *E. coli* and *S. aureus* after different treatments, (scale bar = 200  $\mu\text{m}$ , red

fluorescence indicates ONOO<sup>-</sup> in the bacteria). Levels of SOD oxidase activity in MRSA (k), *E. coli* (l) and *S. aureus* (m) after different treatments ( $n = 3$  independent biological replicates, data are presented as mean  $\pm$  SD). n TUNEL assay representing the DNA damage of MRSA, *E. coli* and *S. aureus* after different treatments, scale bar = 200  $\mu\text{m}$ . Images from three independent biological replicates were acquired, and a representative example is shown in (e), (h), (i), (j) and (n). Control denotes the group received an equal volume of physiological saline followed by either dark or light exposure, whereas Control+D indicates administration of an equal volume of physiological saline followed by dark exposure. D for darkness, L for light. Statistical significance was determined by one-way ANOVA followed by Tukey's post hoc test for multiple comparisons (a, b, c, k, l, and m). Source data are provided as a Source Data file.

mechanisms collapsed due to overwhelming levels of exogenous ROS/NO/RNS, leading to severe structural damage. This trend was also observed for CAT and NOX activities, indicating a comprehensive breakdown of the intracellular redox balance mechanisms. The sustained oxidative stress ultimately resulted in enzyme inactivation and functional failure, significantly contributing to accelerated bacterial cell death.

Finally, targeting bacterial DNA is critical for complete eradication, since bacterial cells have robust DNA repair mechanisms that can promote drug resistance. TUNEL assays (Fig. 6n) confirmed extensive DNA fragmentation in treated groups, with A@Zn-TDP + L exhibiting maximal damage, consistent with ROS/RNS-induced DNA oxidative damage and impaired repair capacity. These findings establish that A@Zn-TDP and A@Ni-TDP disrupt critical cellular processes—membrane integrity, redox balance, and genetic stability—through multimodal mechanisms, providing a comprehensive antibacterial strategy that circumvents conventional resistance pathways.

### Biocompatibility

The safety of medical materials is necessary for their clinical application. To evaluate the cytotoxicity of A@Zn-TDP and A@Ni-TDP, we tested their effects on human umbilical vein endothelial cells (HUVECs) and immortalized human keratinocytes (HaCaT) using the MTT assay (Fig. 7b-c). Even at relatively high concentrations, A@Zn-TDP (50  $\mu\text{g}/\text{mL}$ ) and A@Ni-TDP (250  $\mu\text{g}/\text{mL}$ ) exhibited minimal cytotoxicity, with cell survival rates of  $98.06 \pm 2.92\%$  and  $92.61 \pm 1.11\%$  for HUVECs, and  $98.68 \pm 0.90\%$  and  $94.41 \pm 2.92\%$  for HaCaT cells, respectively. This high cytocompatibility can be attributed to the stable coordination environment of the MOFs and controlled release of reactive species only under light irradiation, minimizing off-target toxicity.

Further confirmation of biocompatibility was provided by live-dead cell staining (Fig. 7a), which showed high cell viability even after 24 and 48 hours of incubation. The absence of red blood cell lysis in hemolysis assays (Supplementary Fig. 35) further supports the biocompatibility of A@Zn-TDP and A@Ni-TDP, suggesting that they are non-hemolytic at therapeutic concentrations. These results collectively affirm the high biosafety and hemocompatibility of both materials within the tested dose range, supporting their potential for topical and systemic applications.

### Cell migration in vitro

Cell migration is a critical process in wound healing, particularly under pathological conditions such as diabetic chronic wounds, where impaired microenvironmental regulation delays recovery<sup>49</sup>. NO has been shown to accelerate healing by promoting endothelial cell proliferation and migration, enhancing microcirculation, and facilitating vasculogenesis through coordinated processes including proliferation, migration, alignment, and tubulogenesis<sup>50</sup>. To evaluate the effects of A@Zn-TDP and A@Ni-TDP on cell migration, scratch assays were performed using HUVECs, with NaNO<sub>2</sub> serving as a NO-release

control. As shown in Fig. 7d and e, both A@Zn-TDP + L and A@Ni-TDP + L significantly enhanced cell migration compared to controls, achieving near-complete scratch closure within 48 hours. The improved migratory behavior is likely mediated by NO-induced activation of pro-healing signaling pathways such as VEGF, which enhance cytoskeletal reorganization and collective cell movement. Notably, A@Zn-TDP and A@Ni-TDP exhibited comparable enhancements in cell migration, suggesting that both materials may effectively promote wound-healing processes through sustained NO release and activation of key regenerative signaling pathways.

### Therapeutic evaluation in diabetic chronic wounds

Building upon the potent anti-biofilm and pro-healing activities of A@Zn-TDP and A@Ni-TDP observed in vitro, we further evaluated their therapeutic efficacy in promoting diabetic chronic wound healing in vivo (Fig. 8a). A type II diabetic mouse model was established using male C57BL/6J mice via high-fat/high-sucrose diet-induced insulin resistance followed by intraperitoneal streptozotocin (STZ) injection. Chronic wounds infected with MRSA biofilms were created on the dorsal skin<sup>51</sup>.

Wound healing assessments revealed that the A@Zn-TDP + L treatment group achieved the most rapid wound closure among all groups tested (Fig. 8b, c, e, f, Supplementary Figs. 36–37, and Supplementary Figs. 39–42). By day 7, wounds treated with A@Zn-TDP + L exhibited a healing rate of  $77.99 \pm 2.67\%$ , markedly surpassing that of the Control+D group ( $47.60 \pm 8.64\%$ ). By day 14, the A@Zn-TDP + L group displayed near-complete closure ( $99.30 \pm 0.19\%$ ), significantly outperforming the Control+D group ( $82.25 \pm 3.79\%$ ), and comparable to the Vancomycin group ( $98.27 \pm 0.60\%$ , with visible open wounds remaining), thereby firmly establishing the effective ability of A@Zn-TDP to accelerate tissue regeneration. Comparable efficacy was observed for A@Ni-TDP, which reached a healing rate of  $98.35 \pm 0.47\%$  by day 14.

Moreover, the Zn-TDP + L group reached a wound closure rate of  $95.88 \pm 1.48\%$  on day 14, significantly higher than that of the PCN-224 + L group ( $87.11 \pm 3.43\%$ ) (Fig. 8b, c, e and f). This result confirms that Zn-TDP, owing to its significantly enhanced photodynamic antibacterial activity, promotes wound healing more effectively than the conventional photosensitizer PCN-224, underscoring the crucial role of rational photosensitizer design—particularly the D-A-D structure with a strong electron-accepting core—in achieving high-efficiency photodynamic antibacterial performance.

Notably, all alternative treatments—including L-Arg+L (dependent solely on endogenous NO derived from iNOS), NaNO<sub>2</sub>+L (exogenous NO donor only), A@Zn-TDP + D (material without light activation), and Zn-TDP + L (ROS generation without NO/RNS)—were consistently less effective than A@Zn-TDP + L (Supplementary Figs. 38). These comparative results underscore the unique advantage of the integrated strategy, in which tetrazine-enhanced photodynamic ROS generation initiates bacterial clearance and biofilm disruption, controllable NO/RNS release penetrates deeper tissue layers to amplify antimicrobial

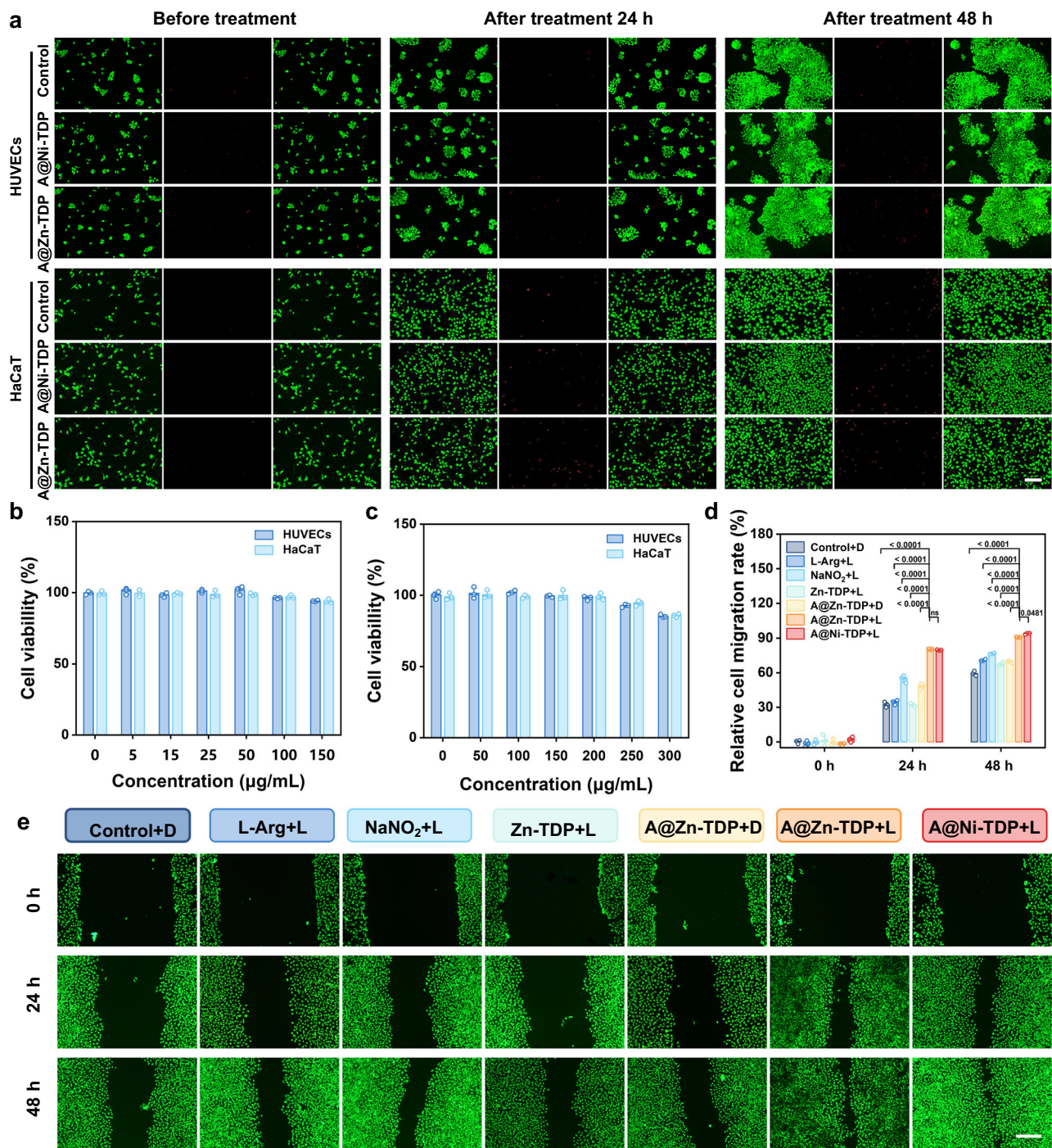


**Fig. 7 | Evaluation of cell safety and migration activities.** **a** Live-dead staining images of HUVECs and HaCaT cells co-cultured with A@Zn-TDP and A@Ni-TDP for 24 and 48 hours, scale bar = 200 µm. MTT assay to determine cell survival of HUVECs and HaCaT after 24 h of co-incubation with A@Ni-TDP (**b**) and A@Zn-TDP (**c**) ( $n = 3$  independent biological replicates, data are presented as mean  $\pm$  SD). **d** Semi-quantitative analysis of HUVECs relative migration rate ( $n = 3$  independent biological replicates, data are presented as mean  $\pm$  SD, statistical significance was

determined by one-way ANOVA followed by Tukey's post hoc test for multiple comparisons). **e** Scratch assay images of HUVECs, scale bars = 200 µm. Images from three independent biological replicates were acquired, and a representative example is shown in (**a**) and (**e**). Control denotes the group received an equal volume of PBS followed by either dark or light exposure, whereas Control+D indicates administration of an equal volume of PBS followed by dark exposure. D for darkness, L for light. Source data are provided as a Source Data file.

and signaling effects, and L-Arg-mediated immunomodulation promotes angiogenesis and tissue remodeling. This combined, multi-pronged approach not only resolves infection but also mitigates inflammation and accelerates tissue regeneration, thereby addressing the multifaceted challenges of chronic and drug-resistant wound healing.

Residual bacterial colony counts within wound tissues (Fig. 8d, g, and Supplementary Fig. 43) collected on day 2 were consistent with the observed healing outcomes. The Zn-TDP + L group achieved a bacterial clearance rate of  $89.45 \pm 1.63\%$ , which was markedly higher than that of the PCN-224 + L group ( $37.29 \pm 5.55\%$ ). Clearance rates were further elevated in the A@Zn-TDP + L ( $98.39 \pm 0.75\%$ ) and A@Ni-TDP + L

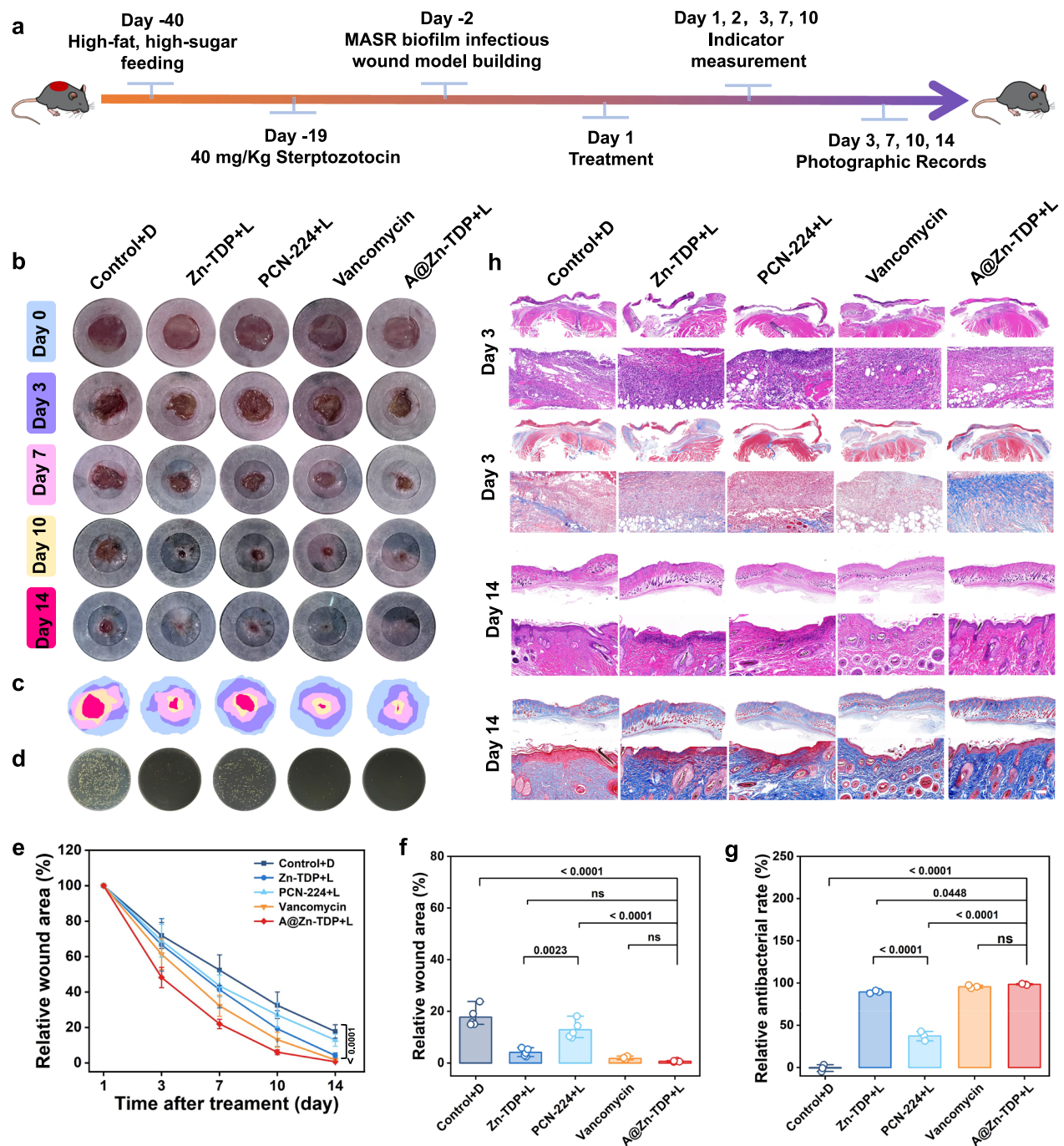


**Fig. 8 | In vivo assessment of promoting chronic wound healing in diabetes mellitus.** **a** Schematic of the animal experimental design. The mouse illustration was adapted from Adult Mouse by Yunan Chen, available on SciDraw (scidraw.io) under a CC BY 4.0 license. **b** Representative photographs showing wound progression in infected mice from the main control and treatment groups over the 14-day treatment period. (Images from one randomly selected mouse per group are shown here; wound photographs of all remaining animals are provided in the Supplementary Information (Supplementary Figs. 37-42). A total of 5 mice per group were included for statistical analysis after randomly excluding those euthanized for pathological assessment.) **c** Wound closure kinetics analyzed using ImageJ. **d** Bacterial colonies cultured from wound tissue homogenates on agar plates, collected on day 2 post-

treatment. **e** Quantitative analysis of wound healing rates throughout the 14-day treatment period ( $n = 5$  independent biological replicates, data are presented as mean  $\pm$  SD). **f** Statistical comparison of wound areas on day 14 after treatment ( $n = 5$  independent biological replicates, data are presented as mean  $\pm$  SD). **g** Quantification of bacterial colony counts from wound samples on day 2 ( $n = 3$  independent biological replicates, data are presented as mean  $\pm$  SD). **h** H&E and Masson's trichrome staining of wound tissues harvested on days 3 and 14 post-treatment (scale bars: 1000  $\mu$ m and 100  $\mu$ m). Control+D indicates administration of an equal volume of physiological saline followed by dark exposure. D for darkness, L for light. Statistical significance was determined by one-way ANOVA followed by Tukey's post hoc test for multiple comparisons (e-g). Source data are provided as a Source Data file.

(95.13  $\pm$  1.04%) groups, approaching near-complete bacterial eradication. These results align closely with the robust in vivo antibiofilm efficacy observed, underscoring the unique advantages of the tetrazine-enhanced MOFs.

Histological analyses further validated these findings: H&E staining (Fig. 8h and Supplementary Fig. 44) showed reduced inflammatory cell infiltration and organized skin architecture in the A@Zn-TDP + L and A@Ni-TDP + L groups by day 3, progressing to nearly intact skin

structures by day 14. Masson's trichrome staining revealed deeper, more organized collagen deposition in these groups, indicative of accelerated tissue regeneration. Finally, consistent increases in body weight (Supplementary Fig. 45a), stable blood glucose levels (Supplementary Fig. 45b), normal histology of major organs (Supplementary Fig. 46), and serum markers of hepatic/renal toxicity (GOT, GPT, UREA, CREA) (Supplementary Figs. 47 and 48) confirmed the favorable *in vivo* biocompatibility of A@Zn-TDP+L and A@Ni-TDP+L treatments.

### Regulatory mechanisms of inflammation and tissue remodeling dynamics

Recent studies<sup>47</sup> indicate that L-Arg-derived NO exerts dual immunomodulatory effects: during early infection, endogenous iNOS-derived NO induce iNOS upregulation and pro-inflammatory cytokine secretion (e.g., TNF- $\alpha$ ), enhancing immune responses against pathogens. Subsequently, elevated NO levels promote Arg-1-mediated conversion of arginine to polyamines, leading to increased anti-inflammatory cytokine secretion (e.g., IL-10) and facilitating the transition from the pro-inflammatory to the anti-inflammatory phase, thereby accelerating tissue repair. To elucidate the mechanisms underlying the therapeutic effects of A@Zn-TDP and A@Ni-TDP during wound healing, we investigated inflammation dynamics in wound tissues collected at days 1, 3, 7, and 14 post-treatment using immunofluorescence double-staining and ELISA quantification.

In the A@Zn-TDP+L group, iNOS expression (Fig. 9a, e) was significantly elevated on day 1 compared to the Control+D group, indicating that initial NO generation induced iNOS upregulation and consequent immune activation. By day 3, iNOS levels markedly declined and continued to decrease significantly below levels in the Control+D group on days 7 and 14. Similarly, TNF- $\alpha$  levels (Fig. 9b, f) were only slightly elevated on day 1, then progressively declined, becoming significantly lower than the Control+D group at later time points. These demonstrate progressive inflammation resolution in the A@Zn-TDP+L group. The marked upregulation of iNOS in the initial phase, coupled with the rapid subsidence of pro-inflammatory markers at later stages, underscores the capacity of A@Zn-TDP+L to dynamically regulate early immune responses while effectively preventing excessive inflammation. Conversely, Arg-1 expression (Fig. 9a, g) in the A@Zn-TDP+L group was slightly higher than the model group on day 1, significantly increased on days 3 and 7, and decreased by day 14. Anti-inflammatory IL-10 expression (Fig. 9b, h) mirrored this trend. This mid-phase upregulation of Arg-1 and IL-10 indicates a timely transition toward pro-regenerative inflammation, driven by sustained NO release and its regulatory effect on immune metabolism. In contrast, other control groups, including Vancomycin, showed gradual increases in Arg-1 and IL-10, but with smaller magnitudes of change, further confirming A@Zn-TDP+L's superior anti-inflammatory modulation. This temporal shift in inflammatory markers suggests a dual-phase therapeutic effect: during the early phase, light-activated NO release enhances iNOS expression and TNF- $\alpha$  production, amplifying immune responses to eliminate bacteria. As bacterial burden diminishes and the pro-inflammatory response subsides, elevated NO levels induce Arg-1 expression, promoting conversion of L-Arg to anti-inflammatory molecules such as polyamines, thereby driving the transition towards tissue repair and resolution of inflammation.

Macrophage polarization analysis further validated this immunomodulatory mechanism (Fig. 9c). On day 1, all groups exhibited prominent CD86<sup>+</sup> (M1) and minimal CD206<sup>+</sup> (M2) signals. By day 3, CD86<sup>+</sup> expression increased across groups but was slightly lower in the A@Zn-TDP+L group, with faint emergence of CD206<sup>+</sup> signal. By day 7, CD86<sup>+</sup> expression decreased markedly—most markedly in the A@Zn-TDP+L group—while CD206<sup>+</sup> signals increased substantially in this treatment group, indicating accelerated M1-to-M2 transition and inflammation resolution.

Importantly, L-Arg+L and NaNO<sub>2</sub>+L groups showed inflammatory marker levels similar to the Control+D group, suggesting that L-Arg or NO alone were insufficient to modulate the wound inflammatory microenvironment effectively. The elevated TNF- $\alpha$  levels observed in Zn-TDP+L and A@Zn-TDP+L groups on day 1 likely resulted from ROS-induced pro-inflammatory stimulation due to efficient tetrazine-enhanced MOF photocatalysis. Hematological analysis (Fig. 9i–k) revealed earlier reduction of inflammatory cells (lymphocytes, neutrophils, leukocytes) in the A@Zn-TDP+L group compared to controls, supporting its effect in promoting systemic inflammation resolution.

Furthermore, immunofluorescence analysis of vascular markers CD31 and  $\alpha$ -SMA on day 14 (Fig. 9d) demonstrated that A@Zn-TDP+L treatment most effectively promoted angiogenesis, with signal intensities following the order: A@Zn-TDP+L > Vancomycin > NaNO<sub>2</sub>+L  $\approx$  Zn-TDP+L > L-Arg+L  $\approx$  A@Zn-TDP+D > Control+D. This enhanced vascularization can be attributed to the combined effects of rapid bacterial clearance and NO-mediated activation of pro-angiogenic pathways.

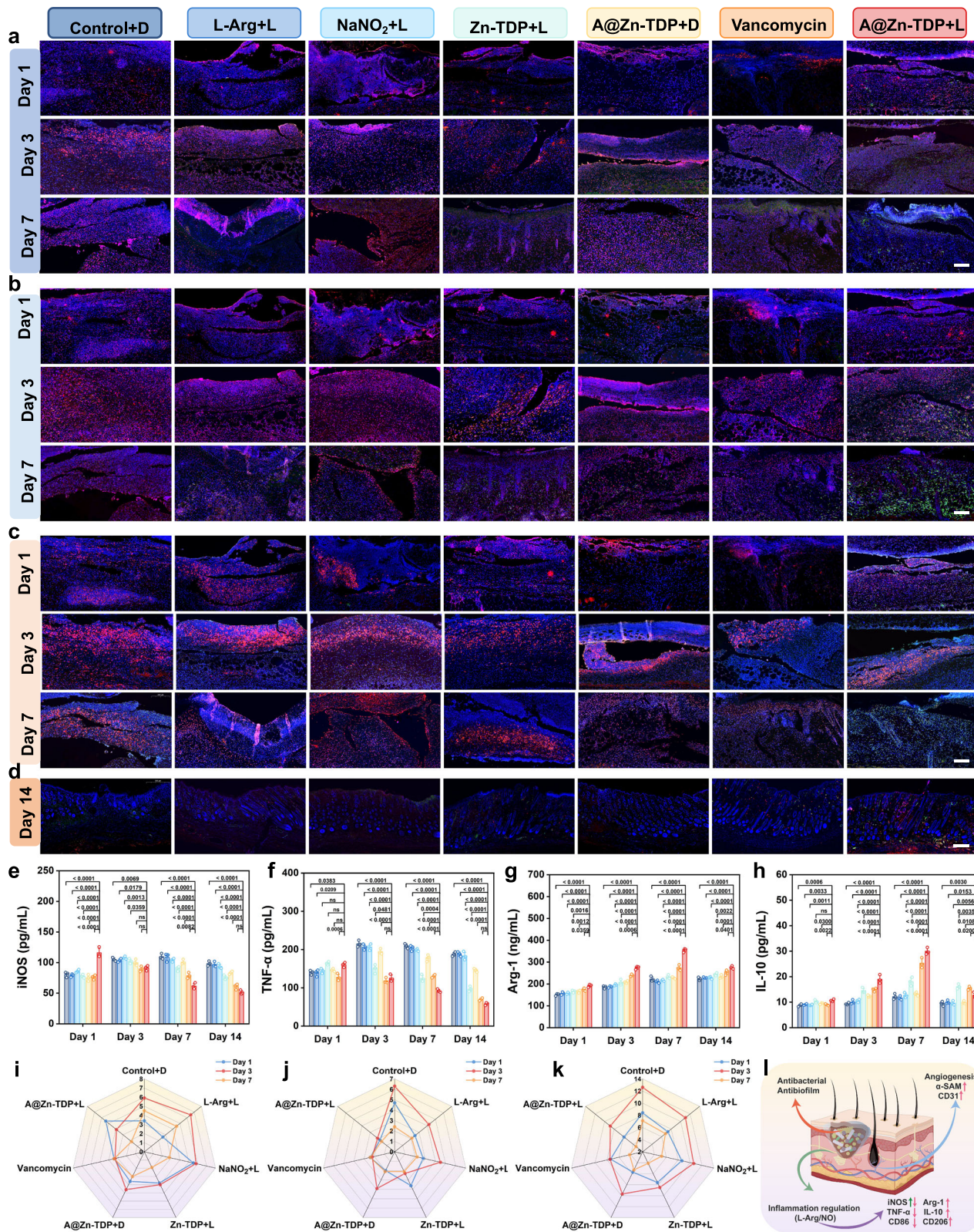
Collectively, these findings indicate that A@Zn-TDP facilitates wound healing through both direct bactericidal effects and sophisticated immunomodulation (Fig. 9l). It initially augments antimicrobial immunity before steering the immune response toward resolution and regeneration, thereby addressing infection and inflammation in a temporally coordinated manner and orchestrating the entire healing process in chronic wounds.

In summary, we have developed tetrazine-enhanced D–A–D photosensitive MOFs—Zn-TDP and Ni-TDP—that utilize an electron-deficient tetrazine core to maximize visible-light absorption and ROS generation. These MOFs exhibit enhanced photodynamic antibacterial performance, outperforming conventional systems such as PCN-224 against drug-resistant bacteria and biofilms, while retaining structural stability suitable for multimodal therapy. By incorporating L-Arg to enable NO gas therapy, the resulting A@Zn-TDP and A@Ni-TDP composites achieve a dual-mode mechanism that combines rapid and potent photodynamic killing with sustained immunomodulation to promote inflammation resolution. This integrated strategy enables low-dose efficacy (25  $\mu$ g/mL), nearly eliminating MRSA *in vitro* and accelerating diabetic wound healing *in vivo*. Our work establishes tetrazine-based D–A–D MOFs as a versatile platform for antimicrobial therapeutics, offering an approach to combat resistant infections and improve the treatment of chronic wounds.

## Methods

### Materials

All chemicals, including zinc acetate dihydrate (Zn(OAc)<sub>2</sub>·2H<sub>2</sub>O), nickel acetate tetrahydrate (Ni(OAc)<sub>2</sub>·4H<sub>2</sub>O), hydrazine hydrate (80%), 2-cyanopyrazole, di-tert-butyl dicarbonate, trifluoroacetic acid, L-arginine, 2-aminoterephthalic acid, Titanium tetrakisopropanolate (TPO), Tetrakis (4-carboxyphenyl) porphyrin (TCPP), Zirconium tetrachloride (ZrCl<sub>4</sub>), 4,4',4'',4'''-(1,9-dihydropyrene-1,3,6,8-tetrayl) tetrabenzoic acid, NaNO<sub>2</sub>, S-Nitrosoglutathione (GSNO), 9,10-Anthraquinonylidenebis(methylene)-dicarboxylic acid (ABDA), Nitro blue tetrazolium chloride (NBT), 8-anilino-1-naphthalenesulfonic acid (ANS), 5,5'-dithiobis(2-nitrobenzoic acid) (DTNB), were purchased from commercial suppliers and used without purification. L-Arg Assay Kit, ROS Assay Kit (DCFH-DA), NO Assay Kit (Griess Reagent), NO fluorescent probe (DAF-FM DA), protease-phosphatase inhibitor mixture, crystal violet staining solution, One-Step TUNEL Apoptosis Assay Kit, and BCA protein quantification kits were sourced from Beyotime Biotechnology (Shanghai, China). LIVE/DEAD Cell Viability Assay Kit, SYTO-9 Live/Dead Bacteria Dual Staining Kit, 2.5% glutaraldehyde fixative, MTT, Citric acid buffer solution (pH=4.5) were purchased from Solarbio (Beijing, China). Calcein AM, propidium iodide, were purchased from Yeasen Biotechnology (Shanghai, China). GOT, GPT, CREA, and UREA



assay Kit were sourced from Beijing Boxbio Science & Technology Co.,Ltd. (Beijing, China). DMEM medium and fetal bovine serum (FBS) were obtained from Tianhang Biotechnology (Zhejiang, China), along with superoxide dismutase (SOD) and catalase (CAT) assay kits, malondialdehyde (MDA) detection kits, bacterial protein extraction kits, and o-nitrophenyl-β-D-galactopyranoside (ONPG).

### Instrumentation

The morphological and structural properties of Zn-TDP, Ni-TDP, A@Zn-TDP, and A@Ni-TDP nanoparticles were analyzed using transmission electron microscopy (TEM, FEI Talos F200X G2, USA) and scanning electron microscopy (SEM, Hitachi Regulus 8100, Japan). Elemental distribution was determined through energy-dispersive

**Fig. 9 | In vivo tissue microenvironment analysis.** **a** Immunofluorescence staining of iNOS (red) and Arg-1 (green) in wound tissues on days 1, 3, and 7 post-treatment (scale bar = 200  $\mu$ m). **b** Immunofluorescence staining of TNF- $\alpha$  (red) and IL-10 (green) on days 1, 3, and 7 (scale bar = 200  $\mu$ m). **c** Immunofluorescence staining of CD86 (red) and CD206 (green) on days 1, 3, and 7 (scale bar = 200  $\mu$ m). **d** Immunofluorescence staining of CD31 (green) and  $\alpha$ -SMA (red) on day 14 (scale bar = 500  $\mu$ m). For **a–c**, the tissue sections showing different indicators for the same treatment group and time point were derived from the same randomly selected representative mouse. **e–h** Cytokine levels in wound tissues quantified by ELISA: **e** iNOS, **f** TNF- $\alpha$ , **g** Arg-1, **h** IL-10. (The colors of each group are the same as

those labeled in **(a–d)**. **i** Lymphocyte counts in blood on days 1, 3, and 7. **j** Neutrophil counts in blood on days 1, 3, and 7. **k** White blood cell (WBC) counts in blood on days 1, 3, and 7. **l** Proposed mechanism of A@Zn-TDP and A@Ni-TDP in wound microenvironment regulation. Control+D indicates administration of an equal volume of physiological saline followed by dark exposure. D for darkness, L for light.  $n = 3$  independent biological replicates, data are presented as mean  $\pm$  SD, statistical significance was determined by one-way ANOVA followed by Tukey's post hoc test for multiple comparisons (**e–h**). Source data are provided as a Source Data file.

X-ray (EDX) mapping using the TEM system. Crystal structures were examined with an X-ray powder diffractometer (Rigaku SmartLab SE, Japan), while chemical compositions were assessed via X-ray photoelectron spectroscopy (XPS, Thermo Scientific K-Alpha, USA). Fourier transform infrared spectroscopy (FT-IR, Tensor 27, Germany) was used to analyze the chemical structures of Zn-TDP, Ni-TDP, A@Zn-TDP, and A@Ni-TDP, and thermal stability was evaluated using a thermogravimetric analyzer (TGA 4000, PerkinElmer, USA). Hydrodynamic size and zeta potential were measured using a Malvern Zetasizer. The specific surface area (BET) was determined using a fully automated specific surface and porosity analyzer (Mike ASAP2460). UV-visible absorption spectra were recorded using a Shimadzu UV-3600 spectrophotometer (Japan), and fluorescence measurements were carried out with a SpectraMax spectrometer (Thermo, USA). Bacterial and intracellular fluorescence were observed using a confocal laser scanning microscope (CLSM, FV3000, Olympus, Japan) and fluorescence inverted microscopy. Electron spin resonance (ESR) measurements were conducted using a Bruker EMXPlus spectrometer (Germany). Light conditions for all experiments were performed under a xenon lamp (Sunlight Analog Filter AML5, Beijing Magnesium Richen Technology Co., China) as the light source.

### Synthesis of organic ligands

**1,4-dipyrazolotetrazine (H<sub>2</sub>TDP)<sup>52</sup>.** 4-Cyanopyrazole (1.00 g, 10.74 mmol) and zinc trifluoromethanesulfonate (0.78 g, 2.14 mmol) were dispersed in 80% hydrazine hydrate (5.21 mL) and reacted under nitrogen at 60 °C for 20 hours. After cooling to room temperature, the mixture was filtered, and the filtrate was collected. An aqueous sodium nitrite solution (5.93 g, 85.92 mmol) was added to the filtrate, and the pH was adjusted to 2–3 using 1 M hydrochloric acid, followed by stirring at room temperature for 6 hours. The resulting solution was filtered, and the filtrate was sequentially washed with water, methanol, and dichloromethane to yield the crude 1,4-dipyrazolium oxidized tetrazine product.

The crude product was then dispersed in dichloromethane, and di-*tert*-butyl dicarbonate (16.11 mmol) was added. The mixture was stirred at room temperature for 30 minutes. After removing the solvent, the residue was purified by flash column chromatography on silica gel (petroleum ether: ethyl acetate = 3: 1), yielding compound B (3.21 g, 7.73 mmol) in 72% yield.

Compound B was dissolved in 20 mL of dichloromethane, and 4 mL of trifluoroacetic acid was added. The mixture was stirred at room temperature for 8 hours, then filtered, and the precipitate was washed with dichloromethane. The solid was transferred to a beaker containing 100 mL of distilled water, and the pH was adjusted to 6–7 using a 0.25 mM sodium hydroxide solution. The solid was filtered again, washed to neutrality with distilled water, and then rinsed with small amounts of ethanol and dichloromethane, yielding a pink solid (6.26 mmol) with an 81% yield. <sup>1</sup>H NMR (400 MHz, *d*<sub>6</sub>-DMSO)  $\delta = 8.53$  (4H, s) (Supplementary Fig. 49). HRMS: *m/z*: 213.0636 [M-H] (Supplementary Fig. 50).

1,4-Dipyrazolylbenzene (H<sub>2</sub>BDP) was synthesized via Suzuki coupling, following established procedures in the literature<sup>39</sup>. BDP-THP: A mixture of 2,5-dibromothiophene (2.5 mmol), 1-(tetrahydro-2H-

pyran-2-yl)-4-(4,4,5,5-tetramethyl-1,3,2-dioxaborolan-2-yl)-1H-pyrazole (6.0 mmol), Cs<sub>2</sub>CO<sub>3</sub> (25 mmol), and Pd(PPh<sub>3</sub>)<sub>4</sub> (0.15 mmol) in dioxane (40 mL) and H<sub>2</sub>O (10 mL) was stirred at 80 °C under N<sub>2</sub> for 72 h. After cooling to room temperature, the mixture was diluted with water and DCM. The aqueous layer was extracted with DCM. The combined organic phases were washed with water and brine, dried and concentrated. The residue was purified by flash column chromatography (petroleum ether/ethyl acetate = 5:1) to afford the protected intermediate BDP-THP.

**H<sub>2</sub>BDP.** To a solution of Ph-Pz-THP (3.65 mmol) in EtOH (20 mL) was added HCl (aq, 1.0 M, 25 mL). The mixture was stirred at 80 °C overnight. After cooling, the precipitate was collected by filtration, washed with ethanol, and then suspended in distilled water (100 mL). The pH was adjusted to 5–7 using NaOH. The resulting solid was filtered, washed with water until neutral, and rinsed with ethanol and ether to give H<sub>2</sub>BDP as an off-white solid. <sup>1</sup>H NMR (400 MHz, *d*<sub>6</sub>-DMSO)  $\delta = 7.58$  (2H, s), 8.06(2H, s) (Supplementary Fig. 51).

### Synthesis of MOFs

**Synthesis of Zn-TDP.** H<sub>2</sub>TDP (214.1 mg, 1.0 mmol) was dispersed in 8 mL of N,N-dimethylformamide (DMF) and stirred for 2 hours. A separate DMF solution of Zn(OAc)<sub>2</sub>·2H<sub>2</sub>O (219.5 mg, 1.0 mmol) was then added, bringing the total volume to 6 mL. Then, the solution was transferred and sealed in 25 mL teflon lined hydrothermal autoclave, which was heated at 80 °C for 21 hours. After cooling to room temperature, the resulting pink solid was collected, washed thoroughly with DMF, methanol, and acetone (centrifugation at 13400  $\times$  g for 15 min), and dried under vacuum for 12 hours to obtain Zn-TDP.

**Synthesis of Ni-TDP.** H<sub>2</sub>TDP (206.4 mg, 0.96 mmol) and Ni(OAc)<sub>2</sub>·4H<sub>2</sub>O (398.1 mg, 1.6 mmol) were dispersed in a mixture of DMF (64 mL) and water (16 mL), then, the solution was transferred and sealed in teflon lined hydrothermal autoclave, which was heated at 150 °C for 21 hours. After completion, the reaction was cooled to room temperature, and the reddish-brown solid was collected. The product was washed with DMF, methanol, and acetone (centrifugation at 13400  $\times$  g for 15 min) and dried under vacuum for 12 hours to yield Ni-TDP.

**Synthesis of Zn-BDP and Ni-BDP.** The synthesis method described above was employed, substituting H<sub>2</sub>TDP with H<sub>2</sub>BDP.

**Synthesis of A@Zn-TDP and A@Ni-TDP.** L-Arg was incorporated into Zn-TDP and Ni-TDP using a standard stirring adsorption method. Zn-TDP (200 mg) and Ni-TDP (200 mg) were each dispersed in 8 mL of anhydrous ethanol. Aqueous L-Arg solution (300 mg in 2 mL) was added dropwise to each dispersion, followed by stirring at room temperature for 12 hours. The resulting solids were collected, washed thoroughly with anhydrous ethanol and water (centrifugation at 13400  $\times$  g for 15 min), and dried under vacuum for 12 hours to yield the final products, A@Zn-TDP and A@Ni-TDP.

Synthesis of PCN-224<sup>53</sup>, NH<sub>2</sub>-MIL-125(Ti)<sup>54</sup>, and NU-1000<sup>55</sup>: The MOFs were synthesized according to literature procedures with the following modifications:

**PCN-224.**  $\text{ZrCl}_4$  (30 mg),  $\text{H}_2\text{TCP}$  (10 mg), and benzoic acid (400 mg) were dissolved in DMF (2 mL) under sonication for 10 minutes. The mixture was heated at 120 °C for 24 hours. After cooling to room temperature, the resulting deep purple crystalline powder was collected by centrifugation, washed repeatedly, and dried.

**NH<sub>2</sub>-MIL-125(Ti).** 2-Aminoterephthalic acid ( $\text{NH}_2\text{-BDC}$ , 1.5 mmol) and acetic acid (0.53 mL) were dissolved in a MeOH/DMF mixed solvent (9:1 v/v, 10 mL total). Titanium isopropoxide (TPOT, 1 mmol) was added, followed by 5 minutes of sonication. The reaction proceeded at 150 °C for 24 hours. The yellow product was isolated by centrifugation, washed, and dried.

**NU-1000.**  $\text{ZrCl}_4$  (0.30 mmol) and benzoic acid (22 mmol) were dissolved in DMF (8 mL) with sonication. The solution was incubated at 80 °C for 1 hour. After cooling,  $\text{H}_4\text{TBApy}$  (0.06 mmol) was added and sonicated for 20 minutes. The yellow suspension was heated at 120 °C for 48 hours. The crystalline product was collected by centrifugation, washed with DMF, then treated with HCl (0.5 mL, 8 M) in DMF (12 mL) at 100 °C for 24 hours. The final yellow powder was collected by centrifugation, sequentially washed with DMF and acetone, soaked in acetone for 12 hours, and dried.

### Electrochemical measurements

The MOF (10 mg) was ground and mixed with 100  $\mu\text{L}$  ethanol and 10  $\mu\text{L}$  Nafion (5.0 wt%) and sonicated for 30 min to yield a dispersed suspension. This suspension was then coated onto fluorine-doped tin oxide (FTO) glass, scraped into a uniform film, and dried in oven for 2 h. Electrochemical measurements were conducted using a CHI-760E workstation with the MOF-coated FTO as the working electrode, Pt wire as the counter electrode, and Ag/AgCl as the reference electrode. Visible light was simulated using a 150  $\text{mW}/\text{cm}^2$  Xe lamp with a UV cutoff filter ( $\lambda \geq 420$  nm) for photocurrent measurements. Photoresponsive signals were recorded at 0.40 V in 0.50 M  $\text{Na}_2\text{SO}_4$  solution, and Mott-Schottky plots were generated at 1000, 2000, and 3000 Hz. Electrochemical impedance spectroscopy (EIS) was performed in 0.50 M  $\text{Na}_2\text{SO}_4$  solution with a sinusoidal wave of 5.0 mV over a frequency range of 100 kHz to 0.05 Hz.

### Detection of ROS, NO, and RNS

**Photocatalytic generation of ROS.** The ability of Zn-TDP and Ni-TDP nanoenzymes to produce ROS, specifically  $^1\text{O}_2$  and  $\text{O}_2^{\cdot-}$ , was evaluated using EPR spectroscopy. Aqueous or methanol suspensions (2 mg/mL) of Zn-TDP and Ni-TDP were sonicated for 10 minutes in the dark. Spin probes, 5,5-dimethyl-1-pyrroline-N-oxide (DMPO) and 2,2,6,6-tetramethyl-1-piperidine (TEMP), were then added to the respective samples, followed by 10 minutes of light irradiation (400–470 nm). After irradiation, samples were immediately analyzed by EPR.

To quantify ROS, we used DCFH-DA as the detection agent. A solution of DCFH-DA in DMSO was treated with 0.01 M NaOH and incubated for 30 minutes at room temperature, protected from light. The reaction was halted by adding phosphate-buffered saline (PBS, pH=7.4), yielding a final DCFH concentration of 10  $\mu\text{M}$ . Experimental groups included L-Arg, Zn-BDP, Zn-TDP, A@Zn-TDP, Ni-BDP, Ni-TDP, and A@Ni-TDP (each at 200  $\mu\text{g}/\text{mL}$ ) mixed with DCFH-DA, while DCFH-DA alone served as the control. Changes in absorbance (500–600 nm) were measured under dark conditions or xenon lamp irradiation (420–780 nm, 150  $\text{mW}/\text{cm}^2$ , 5 min) to assess total ROS production.

**Specific ROS detection.** For superoxide detection, nanoenzyme (100  $\mu\text{g}/\text{mL}$ ) samples were mixed with NBT (100  $\mu\text{g}/\text{mL}$ ) and irradiated with visible light. Samples were collected at 10-minute intervals, and the decrease in NBT absorbance at 259 nm was recorded using a UV-Vis

spectrophotometer. To quantify  $^1\text{O}_2$ , samples were mixed with ABDA, irradiated, and sampled every 5 minutes. The supernatant was diluted 2-fold in PBS and analyzed for absorbance decrease at 400 nm using a UV-Vis spectrophotometer.

**NO release.** NO release from A@Zn-TDP and A@Ni-TDP under light was quantified using a Griess reagent NO detection kit. Under light irradiation conditions (150  $\text{mW}/\text{cm}^2$ , 15 min), the nitric oxide release of materials at different concentrations (100, 200, 300, 400, 500  $\mu\text{g}/\text{mL}$ ) under light exposure conditions (150  $\text{mW}/\text{cm}^2$ , 15 min). Additionally, A@Zn-TDP and A@Ni-TDP (100  $\mu\text{g}/\text{mL}$ ) were tested under different light exposure times (0, 10, 20, 30, 40, 50, 60 min) and light intensities (0, 50, 100, 150, 200  $\text{mW}/\text{cm}^2$ ).

**ONOO<sup>-</sup> detection.** Different materials (PBS, Zn-TDP, A@Zn-TDP, Ni-TDP, A@Ni-TDP) were incubated under dark conditions or irradiated with a xenon lamp (420–780 nm, 150  $\text{mW}/\text{cm}^2$ ) for 10 minutes. An ONOO<sup>-</sup> fluorescent probe (Rhodamine B hydrazide)<sup>46</sup> was then added, incubation continued for 5 min, samples were centrifuged, and changes in the fluorescence emission spectra (500–600 nm) of the supernatant were measured to assess ONOO<sup>-</sup> generation.

**Glutathione oxidation assay.** Glutathione (GSH) oxidizability was assessed using Ellman's reagent (DTNB). A 50 mM DTNB solution in PBS was prepared, and each nanoenzyme sample (Zn-BDP, Zn-TDP, A@Zn-TDP, Ni-BDP, Ni-TDP, and A@Ni-TDP) was mixed with GSH (0.4 mM) at a concentration of 200  $\mu\text{g}/\text{mL}$ . The mixtures were exposed to visible light (150  $\text{mW}/\text{cm}^2$ ) and sampled at 10-minute intervals. After irradiation, DTNB (100 mM) was added to each sample for color development. The supernatant was centrifuged, and the absorbance was measured at 410 nm.

### Antimicrobial activity assay

**Plate coating method.** MRSA, *E. coli*, and *S. aureus* were cultured in LB medium at 37 °C for 12 to 24 hours. The bacterial suspensions were washed three times with saline and diluted to a concentration of 10<sup>8</sup> CFU/mL (OD<sub>600</sub> = 0.1). Each bacterial strain was treated with 1.8 mL of its respective solution containing the following groups:

**MRSA.** Saline, L-Arg (50 mg/mL), Zn-BDP (25  $\mu\text{g}/\text{mL}$ ), Zn-TDP (25  $\mu\text{g}/\text{mL}$ ), A@Zn-TDP (25  $\mu\text{g}/\text{mL}$ ), Ni-BDP (250  $\mu\text{g}/\text{mL}$ ), Ni-TDP (250  $\mu\text{g}/\text{mL}$ ), A@Ni-TDP (250  $\mu\text{g}/\text{mL}$ ),  $\text{H}_2\text{TDP}$  (108  $\mu\text{g}/\text{mL}$ ),  $\text{Ni}(\text{OAc})_2 \cdot 4\text{H}_2\text{O}$  (60  $\mu\text{g}/\text{mL}$ ), and  $\text{Zn}(\text{OAc})_2 \cdot 2\text{H}_2\text{O}$  (11  $\mu\text{g}/\text{mL}$ ), PCN-224 (25  $\mu\text{g}/\text{mL}$ ),  $\text{NH}_2\text{-MIL-125(Ti)}$  (25  $\mu\text{g}/\text{mL}$ ), NU-1000 (25  $\mu\text{g}/\text{mL}$ ).

**E. coli.** Saline, L-Arg (50 mg/mL), Zn-BDP (50  $\mu\text{g}/\text{mL}$ ), Zn-TDP (50  $\mu\text{g}/\text{mL}$ ), A@Zn-TDP (50  $\mu\text{g}/\text{mL}$ ), Ni-BDP (200  $\mu\text{g}/\text{mL}$ ), Ni-TDP (200  $\mu\text{g}/\text{mL}$ ), A@Ni-TDP (200  $\mu\text{g}/\text{mL}$ ),  $\text{H}_2\text{TDP}$  (108  $\mu\text{g}/\text{mL}$ ),  $\text{Ni}(\text{OAc})_2 \cdot 4\text{H}_2\text{O}$  (60  $\mu\text{g}/\text{mL}$ ), and  $\text{Zn}(\text{OAc})_2 \cdot 2\text{H}_2\text{O}$  (11  $\mu\text{g}/\text{mL}$ ), PCN-224 (50  $\mu\text{g}/\text{mL}$ ),  $\text{NH}_2\text{-MIL-125(Ti)}$  (50  $\mu\text{g}/\text{mL}$ ), NU-1000 (50  $\mu\text{g}/\text{mL}$ ).

**S. aureus.** Saline, L-Arg (50 mg/mL), Zn-BDP (25  $\mu\text{g}/\text{mL}$ ), Zn-TDP (25  $\mu\text{g}/\text{mL}$ ), A@Zn-TDP (25  $\mu\text{g}/\text{mL}$ ), Ni-BDP (200  $\mu\text{g}/\text{mL}$ ), Ni-TDP (200  $\mu\text{g}/\text{mL}$ ), A@Ni-TDP (200  $\mu\text{g}/\text{mL}$ ),  $\text{H}_2\text{TDP}$  (108  $\mu\text{g}/\text{mL}$ ),  $\text{Ni}(\text{OAc})_2 \cdot 4\text{H}_2\text{O}$  (60  $\mu\text{g}/\text{mL}$ ), and  $\text{Zn}(\text{OAc})_2 \cdot 2\text{H}_2\text{O}$  (11  $\mu\text{g}/\text{mL}$ ), PCN-224 (25  $\mu\text{g}/\text{mL}$ ),  $\text{NH}_2\text{-MIL-125(Ti)}$  (25  $\mu\text{g}/\text{mL}$ ), NU-1000 (25  $\mu\text{g}/\text{mL}$ ).

All samples were incubated in the dark at 37 °C for 3 hours. Subsequently, they were subjected to either dark or light treatment (420–780 nm, 150  $\text{mW}/\text{cm}^2$ , 15 minutes for Zn-based MOFs and 30 minutes for Ni-based MOFs). Control groups consisted of saline-treated bacteria kept in the dark. Each treated suspension was diluted to 10<sup>5</sup> CFU/mL, and 10  $\mu\text{L}$  was plated on LB agar. Plates were incubated at 37 °C for 12 to 24 hours, and bacterial colonies were counted using ImageJ software.

**Concentration and duration-dependent studies.** Bacterial suspensions ( $10^8$  CFU/mL) were treated with increasing concentrations of Zn-TDP (5, 15, 25, 50, 100  $\mu\text{g/mL}$ ), A@Zn-TDP (5, 15, 25, 50, 100  $\mu\text{g/mL}$ ), and A@Ni-TDP (50, 100, 150, 200, 250, 300  $\mu\text{g/mL}$ ) for 3 hours. After treatment, samples were exposed to light (420–780 nm, 150  $\text{mW/cm}^2$ , 15 minutes for Zn-based and 30 minutes for Ni-based MOFs). Colony counts were performed post-irradiation. Further experiments were conducted using fixed concentrations (MRSA: A@Zn-TDP (25  $\mu\text{g/mL}$ ), A@Ni-TDP (250  $\mu\text{g/mL}$ ); *E. coli*: A@Zn-TDP (50  $\mu\text{g/mL}$ ), A@Ni-TDP (200  $\mu\text{g/mL}$ ); *S. aureus*: A@Zn-TDP (25  $\mu\text{g/mL}$ ), A@Ni-TDP (200  $\mu\text{g/mL}$ )). Colony counts were recorded at varying durations (0, 5, 10, 15, 20, 30, and 40 minutes) and light intensities (0, 50, 100, 150, and 200  $\text{mW/cm}^2$ ).

**Bacterial growth curves.** For growth curve analysis, MRSA was co-incubated with saline, A@Zn-TDP (25  $\mu\text{g/mL}$ ), or A@Ni-TDP (250  $\mu\text{g/mL}$ ) at 37 °C in the dark for 3 hours. *E. coli* was treated with saline, A@Zn-TDP (50  $\mu\text{g/mL}$ ), or A@Ni-TDP (200  $\mu\text{g/mL}$ ), and *S. aureus* was treated similarly (25  $\mu\text{g/mL}$  for A@Zn-TDP, 200  $\mu\text{g/mL}$  for A@Ni-TDP). All samples were then exposed to dark or light conditions, diluted to  $10^5$  CFU/mL, and cultured in LB liquid medium. Optical density at 600 nm (OD<sub>600</sub>) was measured at 2-hour intervals using a microplate reader.

**Live/dead bacterial staining.** Bacterial suspensions treated as described above were centrifuged at 8000 rpm for 5 minutes and stained using the SYTO-9 Live/Dead Bacteria Dual Staining Kit. Fluorescence was observed using an Olympus FV3000 confocal microscope.

**SEM.** Bacterial cells were processed as previously described, centrifuged, and fixed in 2.5% glutaraldehyde at 4 °C for 4 hours. Dehydration was performed using a graded ethanol series (30%, 50%, 70%, 80%, 90%, and 100%) for 15 minutes each. Samples were lyophilized and imaged using a Hitachi Regulus 8100 SEM to observe morphological changes.

#### Anti-biofilm assay

**Crystal violet staining.** MRSA, *E. coli*, and *S. aureus* suspensions ( $2 \times 10^8$  CFU/mL) were added to 24-well plates (4 mL per well) and incubated at 37 °C for 48 hours to form mature biofilms. After washing twice with saline, the biofilms were assigned to the following treatment groups: Control+D, A@Zn-TDP+D, A@Ni-TDP+D, A@Zn-TDP+L, A@Ni-TDP+L. (For *S. aureus* and MRSA, the dosage concentration of A@Zn-TDP was 25  $\mu\text{g/mL}$ , for *E. coli* it was 50  $\mu\text{g/mL}$ , and for all three bacteria, the concentration of A@Ni-TDP was 200  $\mu\text{g/mL}$ .) The samples were incubated at 37 °C for 12 hours, followed by exposure to either dark conditions (D) or visible light irradiation (L) for 30 minutes. After treatment, the supernatant was removed, and the biofilms were washed twice, fixed with 1 mL of methanol for 1 hour, and then treated with an additional 200  $\mu\text{L}$  of methanol for another hour. Next, the wells were drained, and 200  $\mu\text{L}$  of crystal violet dye was added to each well and incubated for 30 minutes. After washing three times, 200  $\mu\text{L}$  of 30% oxalic acid was added, followed by a 30-minute incubation. Digital photographs were taken, and absorbance at 590 nm was measured. The treated biofilm was resuspended in 1 mL of saline, diluted 100-fold, and 10  $\mu\text{L}$  of the dilution was plated onto agar. Bacterial colonies were counted after incubation at 37 °C for 12 to 20 hours.

**Biofilm fluorescence staining.** Bacterial suspensions ( $2 \times 10^8$  CFU/mL) were added to confocal Petri dishes and incubated at 37 °C for 48 hours to promote biofilm formation. Following different treatments, biofilms were stained using the SYTO-9/PI Live/Dead Bacteria Dual Staining Kit and visualized in 3D using an Olympus FV3000 confocal microscope.

**Biofilm flow cytometry analysis.** Bacterial suspension ( $2 \times 10^8$  CFU/mL) was incubated in 24-well plates at 37 °C for 48 hours to allow biofilm formation. After respective treatments, the biofilms were gently washed, disaggregated, and then stained using a SYTO-9/PI Live/Dead Bacterial Viability Kit. The stained bacterial cells were collected by centrifugation, resuspended in 200  $\mu\text{L}$  of saline, and analyzed by flow cytometry. For analysis, a gate was set to exclude debris and select the intact bacterial population. Fluorescence was detected in the FITC channel for SYTO-9 (viable cells) and the PE channel for PI (dead cells). The gating strategy is illustrated in Supplementary Fig. 32.

**SEM.** Biofilm and bacterial morphology were analyzed using SEM. After treatment, the biofilms were fixed with 2.5% glutaraldehyde at 4 °C for 4 hours, followed by dehydration in a graded ethanol series (30%, 50%, 70%, 80%, 90%, and 100%) for 15 minutes at each concentration. Samples were then lyophilized and imaged using a Hitachi Regulus 8100 SEM (Japan) for detailed morphological observation.

#### Peroxidative damage to bacterial cell membranes

**Experimental groups and MDA content analysis.** Five experimental groups were established: Control+D, A@Zn-TDP+D, A@Ni-TDP+D, A@Zn-TDP+L, and A@Ni-TDP+L. MRSA, *E. coli*, and *S. aureus* ( $2 \times 10^8$  CFU/mL) were treated according to these protocols (for *S. aureus* and MRSA, the dosage concentration of A@Zn-TDP was 25  $\mu\text{g/mL}$ , for *E. coli* it was 50  $\mu\text{g/mL}$ , and for all three bacteria, the concentration of A@Ni-TDP was 200  $\mu\text{g/mL}$ ), and malondialdehyde (MDA) content was measured using a malondialdehyde assay kit.

**Outer and inner membrane permeability.** The outer membrane permeability of *E. coli* was evaluated by diluting the bacterial suspension in saline (OD<sub>600</sub> = 0.2) and adding 20  $\mu\text{M}$  ANS. Fluorescence was recorded using an enzyme labeling instrument (excitation: 380 nm; emission: 450–600 nm) and visualized with an inverted fluorescence microscope. Inner membrane permeability changes in MRSA, *E. coli*, and *S. aureus* were assessed using ONPG. Bacterial suspensions (OD<sub>600</sub> = 1.0) were centrifuged, and 100  $\mu\text{L}$  of supernatant was incubated with 100  $\mu\text{L}$  of 10 mM ONPG for 24 hours at room temperature. Absorbance was measured at 420 nm using a microplate reader.

**ROS, NO and ONOO<sup>-</sup> production analysis.** ROS, NO and ONOO<sup>-</sup> production in MRSA, *E. coli*, and *S. aureus* was assessed using DCFH-DA, DAF-FM DA, and Rhodamine B hydrazide<sup>5</sup>, respectively. Bacterial suspensions (OD<sub>600</sub> = 0.25) were divided into Control + D, A@Zn-TDP+D, A@Ni-TDP+D, A@Zn-TDP+L, and A@Ni-TDP+L groups. After a 3-hour co-incubation, the samples were exposed to darkness or light for 10 minutes, and fluorescence was visualized using an Olympus FV3000 confocal microscope.

**Bacterial oxidative stress analysis.** MRSA, *E. coli*, and *S. aureus* (OD<sub>600</sub> = 1.0) were subjected to the same treatment groups. NADH oxidase (NOX) activity was quantified using the NADH Oxidase Activity Assay Kit, while catalase (CAT) activity and superoxide dismutase (SOD) activity were measured using the corresponding kits.

**Bacterial DNA damage assessment.** Bacterial suspensions (OD<sub>600</sub> = 0.25) of MRSA, *E. coli*, and *S. aureus* were treated as described previously. Cells were collected, resuspended in PBS, and stained using a one-step TUNEL assay kit. Fluorescence images were obtained using a confocal laser scanning microscope (CLSM).

#### Biocompatibility and cell migration assays

The Human umbilical vein endothelial cells (HUVECs) (Product #STM-CL-5108) and human keratinocytes (HaCaT) (Product #STM-CL-5186) used in this study were purchased from STEM RECELL Co. (Shanghai, China). They were cultured in DMEM containing 10% fetal bovine

serum (FBS) and antibiotics at 37 °C in a humidified incubator with 5% CO<sub>2</sub>.

**MTT assay.** HUVECs and HaCaT cells were seeded in 96-well plates at a density of  $8 \times 10^3$  cells per well. After 24 hours, the medium was replaced with fresh DMEM containing varying concentrations of A@Zn-TDP (0, 6.25, 12.5, 25, 50, 100 µg/mL) or A@Ni-TDP (0, 25, 50, 100, 150, 200, 250, 300 µg/mL). After another 24-hour incubation, 10 µL of MTT solution (5 mg/mL) was added to each well and incubated for 4 hours at 37 °C. The medium was then removed, and 150 µL of DMSO was added to dissolve the resulting formazan crystals. Absorbance was measured at 570 nm using a microplate reader.

**Live/dead cell staining.** After a 24-hour incubation, cells in 96-well plates were treated with fresh DMEM containing A@Zn-TDP (50 µg/mL) or A@Ni-TDP (250 µg/mL) for 24 or 48 hours. Cell viability was determined using the LIVE/DEAD staining kit (CA1630, Beijing Solepol Technology Co., Ltd.). Staining was performed at baseline, as well as at 24 and 48 hours post-treatment, and visualized using an inverted fluorescence microscope.

**Hemolysis assay.** Red blood cells were collected from healthy ICR mice and diluted in PBS. Each sample (20 µL) was mixed with 1 mL of A@Zn-TDP or A@Ni-TDP at different concentrations (A@Zn-TDP: 0, 12.5, 25, 50, 75, 100, 150 µg/mL; A@Ni-TDP: 0, 50, 75, 100, 150, 200, 250, 300 µg/mL), along with ultrapure water and PBS as positive and negative controls. The mixtures were incubated at 37 °C for 4 hours and centrifuged at 3000 rpm for 15 minutes. Hemoglobin release was measured by the absorbance of the supernatant at 540 nm using a microplate reader, with photographic documentation of the results.

**Scratch assay.** HUVECs were seeded in 96-well plates at  $1 \times 10^5$  cells/well and incubated overnight. A scratch was made in the confluent monolayer. After washing, cells were treated with different agents (blank medium, L-Arg, NaNO<sub>2</sub>, Zn-TDP, A@Zn-TDP, A@Ni-TDP) under dark or light conditions. After 24 or 48 hours, cells were stained with Calcein AM and visualized using an inverted fluorescence microscope.

### Animal experimentation

To standardize for the confounding effects of cyclical estrogen variation on wound healing in females, the study was conducted using healthy male C57BL/6J mice (an inbred strain, 5 weeks of age) supplied by Nanjing Huimiao Biotechnology Co., Ltd. (License No.: SCXK(Wan)2025-0005). Animals were co-housed ( $n = 5$  per cage) in a standardized specific pathogen-free environment with a controlled 12-h light/12-h dark photoperiod, an ambient temperature of  $23 \pm 2$  °C, and 50–60% relative humidity. After one week of acclimatization, insulin resistance was induced through a 4-week regimen of a high-fat/high-sucrose diet. After fasting for 18 hours, mice received intraperitoneal streptozotocin (STZ, 40 mg/kg/day) for four consecutive days. Mice with blood glucose levels  $>16.1$  mmol/L measured over two weeks were considered diabetic. An infected wound model was established under isoflurane anesthesia: an 8-mm dorsal wound was created using a biopsy punch, inoculated with 50 µL MRSA suspension ( $2 \times 10^8$  CFU/mL), and covered with sterile dressing for 2 days to establish biofilm. Diabetic mice were randomly assigned to 10 groups ( $n = 15$ /group): Control+D, L-Arg+L, NaNO<sub>2</sub>+L (NO control), A@Zn-TDP+D, Zn-TDP+L, PCN-224+L, Vancomycin, A@Zn-TDP+L, A@Ni-TDP+L. Treatments were applied under dark or light conditions (PCN-224: 660 nm irradiation; others: visible light, 15 min). To minimize wound contraction, a 3 M silicone ring (10 mm inner diameter, 17 mm outer diameter) was secured around the wound site post-infection using tissue adhesive reinforcement. During the treatment period, mice were randomly selected from each group for euthanasia on days 1, 2, 3, and 7. Skin tissue and other biological samples were collected for

subsequent analyses. Wound areas were photographically documented on days 0, 3, 7, 10, and 14. Ultimately, 5 mice per group underwent the full 14-day monitoring period, with wound area quantified using ImageJ software.

**Bacterial load analysis.** On day 2, one mouse was randomly euthanized. Wound tissue was harvested, homogenized, diluted, and plated on culture dishes for bacterial enumeration.

**Histopathology.** Tissues collected on days 3 and 14 underwent H&E and Masson's trichrome staining.

**Inflammation and angiogenesis.** To investigate healing mechanisms, three mice per time point were randomly selected on days 1, 3, 7, and 14. Tissues were analyzed using ELISA to quantify inflammatory mediators (iNOS, TNF- $\alpha$ , Arg-1, IL-10;  $n = 3$  biological replicates) and subjected to immunofluorescence double-staining for iNOS/Arg-1, TNF- $\alpha$ /IL-10, and CD86/CD206 expression. At the same time, peripheral blood samples were collected on days 1, 3, and 7 for white blood cell count analysis (WBC, neutrophils, lymphocytes, monocytes) to evaluate the systemic inflammatory response. Neovascularization on day 14 was assessed by CD31/ $\alpha$ -SMA immunofluorescence. Pathological sections were prepared by Nanjing Youmeng Biotechnology Co., Ltd.

**Systemic safety assessment.** Monitor and record the body weight and blood glucose levels of mice throughout the entire treatment cycle. On day 14, major organs (heart, liver, spleen, lungs, and kidneys) were collected randomly from mice for H&E staining. Serum samples were obtained to measure biomarkers (GOT, GPT, urea, creatinine) for toxicity assessment.

### Statistics and reproducibility

All quantitative data represent the mean  $\pm$  SD of  $\geq 3$  independent replicates. Statistical analyses were performed in GraphPad Prism 9, with significant differences evaluated by one-way ANOVA followed by Tukey's test. Data visualization was done using Origin 2021.

### Ethical statement

All animal procedures were approved by the Animal Care and Use Committee of China Pharmaceutical University (2025-02-105), and complied with international welfare guidelines.

### Reporting summary

Further information on research design is available in the Nature Portfolio Reporting Summary linked to this article.

### Data availability

The authors declare that all the data supporting the findings of this study are available within the article and supplementary information. Source data are provided with this paper.

### References

1. Jernigan, J. A. et al. Multidrug-Resistant Bacterial Infections in U.S. Hospitalized Patients, 2012–2017. *N. Engl. J. Med.* **382**, 1309–1319 (2020).
2. Kalelkar, P. P., Riddick, M. & García, A. J. Biomaterial-based antimicrobial therapies for the treatment of bacterial infections. *Nat. Rev. Mater.* **7**, 39–54 (2022).
3. Dickey, S. W., Cheung, G. Y. C. & Otto, M. Different drugs for bad bugs: antivirulence strategies in the age of antibiotic resistance. *Nat. Rev. Drug Discov.* **16**, 457–471 (2017).
4. Ikuta, K. S. et al. Global mortality associated with 33 bacterial pathogens in 2019: a systematic analysis for the Global Burden of Disease Study 2019. *Lancet* **400**, 2221–2248 (2022).

5. Murray, C. J. L. et al. Global burden of bacterial antimicrobial resistance in 2019: a systematic analysis. *Lancet* **399**, 629–655 (2022).
6. Sati, H. et al. The WHO Bacterial Priority Pathogens List 2024: a prioritisation study to guide research, development, and public health strategies against antimicrobial resistance. *Lancet Infect. Dis.* **25**, 1033–1043 (2025).
7. Methicillin-resistant *Staphylococcus aureus*. *Nat. Rev. Dis. Primer* **4**, 1–1 (2018).
8. Turner, N. A. et al. Methicillin-resistant *Staphylococcus aureus*: an overview of basic and clinical research. *Nat. Rev. Microbiol.* **17**, 203–218 (2019).
9. Theuretzbacher, U., Outterson, K., Engel, A. & Karlén, A. The global preclinical antibacterial pipeline. *Nat. Rev. Microbiol.* **18**, 275–285 (2020).
10. Rumbaugh, K. P. & Sauer, K. Biofilm dispersion. *Nat. Rev. Microbiol.* **18**, 571–586 (2020).
11. Gupta, P., Sarkar, S., Das, B., Bhattacharjee, S. & Tribedi, P. Biofilm, pathogenesis and prevention—a journey to break the wall: a review. *Arch. Microbiol.* **198**, 1–15 (2016).
12. Mei, J. et al. Biofilm microenvironment-responsive self-assembly nanoreactors for all-stage biofilm associated infection through bacterial cuproptosis-like death and macrophage re-rousing. *Adv. Mater.* **35**, 2303432 (2023).
13. Qin, M. et al. Engineered probiotic bio-heterojunction with robust antibiofilm modality via “eating” extracellular polymeric substances for wound regeneration. *Adv. Mater.* **36**, 2402530 (2024).
14. Simon, M., Aristidis, V. & David, J. M. Advanced bandages for diabetic wound healing. *Sci. Transl. Med.* **13**, eabe4839 (2021).
15. Vartanian, A. Helping diabetic wounds heal. *Nat. Rev. Mater.* **9**, 845–845 (2024).
16. Sun, Y. et al. A hemoglobin bionics-based system for combating antibiotic resistance in chronic diabetic wounds via iron homeostasis regulation. *Adv. Mater.* **36**, 2405002 (2024).
17. Wan, Y., Fu, L.-H., Li, C., Lin, J. & Huang, P. Conquering the hypoxia limitation for photodynamic therapy. *Adv. Mater.* **33**, 2103978 (2021).
18. Ran, B. et al. Photocatalytic antimicrobials: principles, design strategies, and applications. *Chem. Rev.* **123**, 12371–12430 (2023).
19. He, C. et al. Nanomaterials in antibacterial photodynamic therapy and antibacterial sonodynamic therapy. *Adv. Funct. Mater.* **34**, 2402588 (2024).
20. Li, X. et al. Phthalocyanines as medicinal photosensitizers: Developments in the last five years. *Coord. Chem. Rev.* **379**, 147–160 (2019).
21. Lo, P.-C. et al. The unique features and promises of phthalocyanines as advanced photosensitizers for photodynamic therapy of cancer. *Chem. Soc. Rev.* **49**, 1041–1056 (2020).
22. Park, J. M., Hong, K.-I., Lee, H. & Jang, W.-D. Bioinspired applications of porphyrin derivatives. *Acc. Chem. Res.* **54**, 2249–2260 (2021).
23. Zhang, T., Ma, C., Sun, T. & Xie, Z. Unadulterated BODIPY nanoparticles for biomedical applications. *Coord. Chem. Rev.* **390**, 76–85 (2019).
24. Xiong, X. et al. Self-assembly strategies of organic small-molecule photosensitizers for photodynamic therapy. *Coord. Chem. Rev.* **510**, 215863 (2024).
25. Zhao, X., Liu, J., Fan, J., Chao, H. & Peng, X. Recent progress in photosensitizers for overcoming the challenges of photodynamic therapy: from molecular design to application. *Chem. Soc. Rev.* **50**, 4185–4219 (2021).
26. Wang, D. et al. Synthesis of self-assembled porphyrin nanoparticle photosensitizers. *ACS Nano* **12**, 3796–3803 (2018).
27. Zheng, Q. et al. The recent progress on metal–organic frameworks for phototherapy. *Chem. Soc. Rev.* **50**, 5086–5125 (2021).
28. Li, J. et al. 2D MOF periodontitis photodynamic ion therapy. *J. Am. Chem. Soc.* **143**, 15427–15439 (2021).
29. Wu, M.-X. & Yang, Y.-W. Metal–organic framework (MOF)-based drug/cargo delivery and cancer therapy. *Adv. Mater.* **29**, 1606134 (2017).
30. Li, S.-Y. et al. Cancer cell membrane camouflaged cascade bio-reactor for cancer targeted starvation and photodynamic therapy. *ACS Nano* **11**, 7006–7018 (2017).
31. Wang, S. et al. PDI bridged MIL-125(Ti)-NH<sub>2</sub> heterojunction with frustrated Lewis pairs: A promising photocatalyst for Cr(VI) reduction and antibacterial application. *Appl. Catal. B Environ.* **317**, 121798 (2022).
32. Jiao, L., Wang, Y., Jiang, H.-L. & Xu, Q. Metal–organic frameworks as platforms for catalytic applications. *Adv. Mater.* **30**, 1703663 (2018).
33. Zou, Y. et al. Strategy to efficient photodynamic therapy for anti-bacterium: donor-acceptor structure in hydrogen-bonded organic framework. *Adv. Mater.* **36**, 2406026 (2024).
34. Xu, R. et al. Less is more: asymmetric D–A type agent to achieve dynamic self-assembled nanoaggregates for long-acting photodynamic therapy. *Adv. Mater.* **36**, 2402434 (2024).
35. Hao, B. et al. Bridging D–A type photosensitizers with the azo group to boost intersystem crossing for efficient photodynamic therapy. *Chem. Sci.* **13**, 4139–4149 (2022).
36. Yu, M.-H., Geng, L., Chang, Z. & Bu, X.-H. Coordination bonding directed molecular assembly toward functional metal–organic frameworks: from structural regulation to properties modulation. *Acc. Mater. Res.* **4**, 839–853 (2023).
37. Gehring, J. et al. Sunlight-triggered nanoparticle synergy: teamwork of reactive oxygen species and nitric oxide released from mesoporous organosilica with advanced antibacterial activity. *J. Am. Chem. Soc.* **138**, 3076–3084 (2016).
38. He, T. et al. Trace removal of benzene vapour using double-walled metal–dipyrazolate frameworks. *Nat. Mater.* **21**, 689–695 (2022).
39. Wu, K. et al. Linker engineering for reactive oxygen species generation efficiency in ultra-stable nickel-based metal–organic frameworks. *J. Am. Chem. Soc.* **145**, 18931–18938 (2023).
40. Zadehnazari, A., Khosropour, A., Altaf, A. A., Rosen, A. S. & Abbas-pourrad, A. Tetrazine-linked covalent organic frameworks with acid sensing and photocatalytic activity. *Adv. Mater.* **36**, 2311042 (2024).
41. Zhang, H., Lin, Z., Kidkhunthod, P. & Guo, J. Stable Immobilization of Nickel Ions on Covalent Organic Frameworks for Panchromatic Photocatalytic Hydrogen Evolution. *Angew. Chem. Int. Ed.* **62**, e202217527 (2023).
42. Mohammadnezhad, G. et al. Dinuclear Nickel(II) and Copper(II) Complexes of 8-Quinoline-1H-pyrazole-3-carboxamide: Crystal Structure, Magnetic Properties, and DFT Calculations. *Eur. J. Inorg. Chem.* **2021**, 1786–1795 (2021).
43. The one-electron transfer redox potentials of free radicals. I. The oxygen/superoxide system. *Biochim. Biophys. Acta BBA - Bioenerg.* **430**, 209–224 (1976).
44. Jin, J.-K. et al. Building a pyrazole–benzothiadiazole–pyrazole photosensitizer into metal–organic frameworks for photocatalytic aerobic oxidation. *J. Am. Chem. Soc.* **143**, 21340–21349 (2021).
45. Wang, T.-Y., Zhu, X.-Y. & Wu, F.-G. Antibacterial gas therapy: Strategies, advances, and prospects. *Bioact. Mater.* **23**, 129–155 (2023).
46. Ambikapathi, G. et al. Bioimaging of Peroxynitrite in MCF-7 Cells by a New Fluorescent Probe Rhodamine B Phenyl Hydrazide. *J. Fluoresc.* **23**, 705–712 (2013).
47. Zhang, A. et al. Targeting and arginine-driven synergizing photodynamic therapy with nutritional immunotherapy nanosystems for combating MRSA biofilms. *Sci. Adv.* **9**, eadg9116 (2023).
48. Qin, J. et al. Bionic Microneedle Patch Inspired by *Drosophila* Tarsal Paws Boosts Healing in Bacterial Infectious Stomatitis. *Adv. Sci.* e00432.

49. Chen, S. et al. In-situ-sprayed therapeutic hydrogel for oxygen-actuated Janus regulation of postsurgical tumor recurrence/metastasis and wound healing. *Nat. Commun.* **15**, 814 (2024).
50. Su, L. et al. Low-temperature trigger nitric oxide nanogenerators for anti-biofilm and wound healing. *Adv. Fiber Mater.* **6**, 512–528 (2024).
51. Yang, L. et al. Biofilm microenvironment triggered self-enhancing photodynamic immunomodulatory microneedle for diabetic wound therapy. *Nat. Commun.* **14**, 1–17 (2023).
52. Choi, S.-K., Kim, J. & Kim, E. Overview of syntheses and molecular-design strategies for tetrazine-based fluorogenic probes. *Molecules* **26**, 1868 (2021).
53. Feng, D. et al. Construction of ultrastable porphyrin Zr metal–organic frameworks through linker elimination. *J. Am. Chem. Soc.* **135**, 17105–17110 (2013).
54. Cheng, X.-M., Dao, X.-Y., Wang, S.-Q., Zhao, J. & Sun, W.-Y. Enhanced Photocatalytic CO<sub>2</sub> Reduction Activity over NH<sub>2</sub>-MIL-125(Ti) by Facet Regulation. *ACS Catal.* **11**, 650–658 (2021).
55. Mondloch, J. E. et al. Vapor-phase metalation by atomic layer deposition in a metal–organic framework. *J. Am. Chem. Soc.* **135**, 10294–10297 (2013).

## Acknowledgements

The authors are gratefully thankful for the support from Science and Technology Department of Fujian Province Pilot Project (2022Y0019, W.C.Q), Fujian Provincial Department of Finance Special Project Funds (2024CZ006, W.C.Q), Natural Science Foundation of Jiangsu Province, China (BK20221047, J.X.C), the Fundamental Research Funds for the Central Universities (2632025ZD07, J.X.C). We thank Dr. Huimin Xu of The Public Laboratory Platform at China Pharmaceutical University for assistance with NMR techniques.

## Author contributions

W.W.G proposed the research concept, guided the experimental design, and oversaw the manuscript writing and revision. Y.Q.Z and W.C.Q provided the experimental platform and advised on the writing and correction of the manuscript. Y.Z.C participated in the design and conception of the study, was responsible for the design and implementation of the experimental protocols, and completed the initial draft writing and subsequent revisions. Y.Y.X took part in the implementation of various experimental schemes and contributed to experimental data processing and manuscript revision. X.W.X engaged in the synthesis of related compounds. Y.S participated in the determination of electrochemical parameters, X.D.T synthesized the RNS fluorescent probes, L.Z contributed to the processing of experimental data, Y.F.Z and C.B

assisted in animal experimental research, and J.X.C participated in the animal experiments. The manuscript was written through contributions of all authors. All authors have given approval to the final version of the manuscript.

## Competing interests

The authors declare no competing interests.

## Additional information

**Supplementary information** The online version contains supplementary material available at <https://doi.org/10.1038/s41467-025-65527-z>.

**Correspondence** and requests for materials should be addressed to Wancai Que, Yueqin Zheng or Weiwei Guo.

**Peer review information** *Nature Communications* thanks Chen Yang, and the other, anonymous, reviewer(s) for their contribution to the peer review of this work. A peer review file is available.

**Reprints and permissions information** is available at <http://www.nature.com/reprints>

**Publisher's note** Springer Nature remains neutral with regard to jurisdictional claims in published maps and institutional affiliations.

**Open Access** This article is licensed under a Creative Commons Attribution-NonCommercial-NoDerivatives 4.0 International License, which permits any non-commercial use, sharing, distribution and reproduction in any medium or format, as long as you give appropriate credit to the original author(s) and the source, provide a link to the Creative Commons licence, and indicate if you modified the licensed material. You do not have permission under this licence to share adapted material derived from this article or parts of it. The images or other third party material in this article are included in the article's Creative Commons licence, unless indicated otherwise in a credit line to the material. If material is not included in the article's Creative Commons licence and your intended use is not permitted by statutory regulation or exceeds the permitted use, you will need to obtain permission directly from the copyright holder. To view a copy of this licence, visit <http://creativecommons.org/licenses/by-nc-nd/4.0/>.

© The Author(s) 2025